A new process-based and scale-aware desert dust emission scheme for global climate models – Part II: evaluation in the Community Earth System Model (CESM2)

5   Danny M. Leung[1], Jasper F. Kok[1], Longlei Li[2], Natalie M. Mahowald[2], David M. Lawrence[3], Simone Tilmes[3], Erik Kluzek[3], Martina Klose[4], and Carlos Pérez García-Pando[5,6]

[1]Department of Atmospheric and Oceanic Sciences, University of California – Los Angeles, Los Angeles, California, USA
10   [2]Department of Earth and Atmospheric Sciences, Cornell University, Ithaca, New York, USA
[3]National Center for Atmospheric Research, Boulder, Colorado, USA
[4]Department Troposphere Research, Institute of Meteorology and Climate Research (IMK-TRO), Karlsruhe Institute of Technology (KIT), Karlsruhe, Germany
[5]Barcelona Supercomputing Center (BSC), Barcelona, Spain
15   [6]Catalan Institution for Research and Advanced Studies (ICREA), Barcelona, Spain

Correspondence to: Danny M. Leung (dannymleung@ucla.edu)

20   **Abstract**

Desert dust is an important atmospheric aerosol that affects the Earth's climate, biogeochemistry, and air quality. However, current Earth system models (ESMs) struggle to accurately capture the impact of dust on the Earth's climate and ecosystems, in part because these models lack several essential aeolian
25   processes that couple dust with climate and land surface processes. In this study, we address this issue by implementing several new parameterizations of aeolian processes detailed in our companion paper into the Community Earth System Model version 2 (CESM2). These processes include (1) incorporating a realistic soil particle size distribution to calculate the dust emission threshold friction velocity, (2) accounting for the drag partition effect of rocks and vegetation in reducing wind stress on erodible soils,
30   (3) accounting for the intermittency of dust emissions due to unresolved turbulent wind fluctuations, and (4) correcting the spatial variability of simulated dust emissions from native to higher spatial resolutions on spatiotemporal dust variability. Our results show that the modified dust emission scheme significantly reduces the model bias against observations compared to the default scheme and improves the correlation against observations of multiple key dust variables such as dust aerosol optical depth (DAOD), surface
35   particulate matter (PM) concentration, and deposition flux. Our scheme's dust also correlates strongly with various meteorological and land surface variables, implying higher sensitivity of dust to future climate change than other schemes' dust. These findings highlight the importance of including additional aeolian processes for improving the performance of ESM aerosol simulations and potentially enhancing model assessments of how dust impacts climate and ecosystem changes.
40

1 Introduction

Desert dust is responsible for over half of the atmospheric mass loading of particulate matter (PM)
45   (Kinne et al., 2006; Kok et al., 2017) and produces multiple impacts on the Earth system. Dust contributes to the aerosol radiative effect and forcings directly by absorbing and scattering solar and terrestrial radiation (Di Biagio et al., 2020; Ke et al., 2022; Adebiyi et al., 2023; Kok et al., 2023), and indirectly by

regulating liquid and ice cloud formation (e.g., McGraw et al., 2020; Froyd et al., 2022). Furthermore, dust provides essential nutrients such as iron and phosphorus to terrestrial and ocean ecosystems, thereby promoting biogeochemical activities and enhancing ecosystem carbon uptake (e.g., Mahowald et al., 2010; Hamilton et al., 2020). However, dust also causes pulmonary and cardiovascular diseases, posing a threat to human health (e.g., Esmaeil et al., 2014; Goudie, 2014; Achakulwisut et al., 2019). Despite its significance, global climate models (GCMs) and Earth system models (ESMs) still face challenges in accurately simulating the spatiotemporal distribution of dust aerosols (Zhao et al., 2022), leading to significant uncertainties in the assessments of their climatic impacts (Klose et al., 2021; Li et al., 2021). Current models also struggle to simulate the impacts of how past and future climate and land use changes impact dust emissions (Kok et al., 2023). Therefore, it is critical to improve dust simulations to better predict future dust changes and better simulate dust impacts on climate and climate change.

The difficulty that GCMs and ESMs face in capturing the spatiotemporal variability of atmospheric dust can be attributed to two main factors. First, current dust emission parameterizations in ESMs are likely conceptually incomplete. There is still a limited understanding of dust emission mechanics, and several aeolian processes are not yet included in model parameterizations. For instance, the wind drag partition effect due to the presence of nonerodible roughness elements, interparticle forces due to soil microbes (Rodriguez-Caballero et al., 2018), and human impacts such as agriculture (e.g., Kandakji et al., 2020; Xia et al., 2022) on dust emission are not accounted for in many existing ESM dust parameterizations. As a result, many ESMs use preferential source masks (e.g., Ginoux et al., 2001; Zender et al., 2003a) to eliminate dust from marginal regions. Second, the existing dust emission parameterizations are not well constrained due to inadequate information and constraints on relevant parameters. For example, past studies show that the dust emission threshold wind speed should be modeled using a median soil particle diameter D_p (Martin and Kok, 2019). Leung et al. (2022) used soil data previous studies to show that the median D_p is about ~130 μm, in contrast to the existing parameter range of 75–500 μm (e.g., Zender et al., 2003a; Laurent et al., 2008). Furthermore, many meteorological and land surface variables such as wind speed and soil moisture, which dust emissions are heavily dependent on (Zender et al., 2003a), are challenging to model well in ESMs. There is a need to improve dust emission modeling in ESMs by incorporating more physical aeolian processes and setting more accurate parameter constraints.

Additionally, dust modeling in GCMs and ESMs suffers from a grid resolution-dependence problem, especially since dust emissions depend nonlinearly on meteorological and land surface fields (Feng et al., 2022). Coarse GCMs with horizontal resolutions of 100 km cannot capture local-scale (~1km scale) wind maxima, leading to an underestimation of emissions over specific regions (Ridley et al., 2013; Gliß et al., 2021; Meng et al., 2021). This scale dependence problem is exacerbated by dust emission being a threshold process that scales with friction velocity u_* to the power of ~2–4, resulting in dust emission schemes being further sensitive to inaccuracies in wind speed and other input data (such as soil moisture and vegetation cover). Although some ESMs employ a Weibull distribution to address the subgrid spatial variability of winds (e.g., Menut, 2018), it is challenging to represent the shape parameter k of the Weibull distribution because of a lack of fine-resolution global wind datasets to calibrate a global distribution of k (Tai et al., 2021). Moreover, many GCMs simply do not employ any subgrid wind distribution to address the scale-dependence problem. In addition, other meteorological and land surface variables such as soil moisture and vegetation also contribute to the scale-dependence problem of dust emissions. To improve the accuracy of simulations and to make ESM dust emission simulations self-consistent across different horizontal grid resolutions, it is crucial to address and mitigate this scale-dependence problem.

95   In our companion paper (Leung et al., 2022), we presented four improvements to enhance the physical realism of dust emission parameterizations in ESMs. These include: 1) a revised soil median diameter for better estimating the dust emission threshold, 2) a drag partition scheme considering the impacts of both rocks and vegetation in reducing soil erosion by winds, 3) a dust emission intermittency parameterization accounting for boundary-layer turbulent wind fluctuations that initiate and cease dust

100 emissions, and 4) an upscaling approach to correct the spatial variability of dust emissions from native-resolution ESMs to match that of high-resolution dust emission simulations, with the collective aim of these improvements to better capture the subgrid spatial variations of dust emissions. Our implemented scheme contains updated and more comprehensive dust emission processes. We will examine in this study how including more aeolian processes will benefit dust modeling performance.

105

   In this study, we integrate the improved dust emission scheme from Leung et al. (2022) into a premier ESM, the Community Earth System Model version 2 (CESM2). We describe the default and the updated dust emission modules in Sects. 2 and 3, respectively. In Sect. 4, we provide an overview of the observational and reanalysis datasets used to assess the effectiveness of our new scheme, including

110 datasets of dust aerosol optical depth (DAOD), dust PM concentration, and dust deposition flux. In Sect. 5, we then evaluate the new dust emission scheme by comparing the simulations against observations. We summarize our study in Sect. 6.

2 Description of CESM2 and its default dust scheme

115

   In this section, we summarize the default schemes and settings in CESM2. Section 2.1 describes the default dust emission scheme in the Community Land Model version 5 (CLM5), the land component of CESM2, including the dust emission threshold scheme (Sect. 2.1.1) and the emission flux parameterization (Sect. 2.1.2). Section 2.2 summarizes the atmospheric dust simulation in the Community

120 Atmosphere Model version 6 (CAM6), the atmospheric component of CESM2, including transport, size distribution, and deposition. Section 2.3 describes the CESM2 configuration in this study.

2.1 Default CESM2 dust emission scheme

125 **2.1.1 Dust emission threshold scheme**

   Recent findings indicated that the dust emission process is a double-threshold mechanics problem (Kok et al., 2012; Comola et al., 2019). The fluid threshold u_{*ft} is the threshold friction velocity above which winds initiate emissions, whereas the impact threshold u_{*it} is the threshold friction velocity below which winds are too weak to sustain emissions (Kok et al., 2012). Without considering the soil moisture

130 effect on the fluid threshold, u_{*it} is about 80 % of the "dry" fluid threshold u_{*ft0} (Sect. 3.4; Kok et al., 2012; Comola et al., 2019). Nevertheless, most dust emission schemes in global and regional models employ u_{*ft} as the single threshold for both the initiation and termination of dust emission flux in models (Menut et al., 2013; Klose et al., 2021; Tai et al., 2021; Li et al., 2022; LeGrand et al., 2023), which could be problematic (see Sect. 3.4). The current u_{*ft} parameterization scheme assumes that u_{*ft} is dependent

135 on the particle size distribution (PSD) and the amount of moisture in the soil (Iversen and White, 1982; Marticorena and Bergametti, 1995; Zender et al., 2003a). u_{*ft} is modeled as follows:

$$u_{*ft} = u_{*ft0}(D_p, \rho_a)f_m(w) \tag{1}$$

where u_{*ft0} is the "dry" fluid threshold friction velocity (in m s^{-1}) with no soil moisture on a smooth and bare surface. u_{*ft0} is a function of D_p, which in this study will be the median diameter of a mixed soil,

140 and ρ_a the air density (kg m^{-3}). f_m is the correction factor for the presence of gravimetric soil moisture w (kg water / kg soil); $f_m \geq 1$ such that soil moisture protects soil particles from being lifted. u_{*ft} is the

"wet" fluid threshold accounting for the moisture effect. We note that other factors can also affect u_{*ft}, such as salt concentration, electrostatics (Kok and Renno, 2009), and surface crusts (Rodriguez-Caballero et al., 2022), but most of these factors are not included in most modeling studies because they are not well understood and modeled (Shao et al., 2011; Foroutan et al., 2017).

The variables in Eq. 1 are computed as follows. First, u_{*ft0} is parameterized in CLM following the Iversen and White (1982; hereafter I&W82) scheme (Oleson et al., 2013) as a function of D_p and ρ_a. CLM5 uses a global optimal soil diameter of $D_p = 75\ \mu$m for the threshold calculation (Zender et al., 2003), and thus the spatiotemporal variability of u_{*ft0} purely follows that of ρ_a. Then, CLM5 calculates f_m, the effect of soil moisture on enhancing u_{*ft} following Fécan et al. (1999). f_m is a function of the difference between the gravimetric soil moisture w (kg water / kg soil) and a threshold value w_t. $f_m > 1$ once gravimetric moisture is bigger than w_t, leading to an increase in u_{*ft}:

$$f_m = \sqrt{1 + 1.21(w - w_t)^{0.68}} \qquad \text{for } w > w_t \qquad (2a)$$
$$w_t = a(0.17 f_{clay} + 0.0014 f_{clay}^2) \qquad (2b)$$

where a is a tunable constant typically around 0.5–2 (Kok et al., 2014b) and is set to be $1/f_{clay}$ for tuning purposes in CLM5 (Oleson et al., 2013). The threshold moisture w_t increases with clay fraction $f_{clay} \in [0,1]$, since clay efficiently adsorbs water such that more moisture is required to enhance u_{*ft}. CLM5 currently uses the soil texture dataset from the Food and Agriculture Organization (FAO) for f_{clay}, but will likely update to more recent datasets (e.g., SoilGrids; Hengl et al., 2017) in the future.

2.1.2 Dust emission flux calculation

After obtaining u_{*ft}, there are multiple published dust emission equations that relate the global dust emission flux to a given u_{*ft} and friction velocity u_* (Gillette and Passi, 1988; Shao et al., 1996; Ginoux et al., 2001; Zender et al., 2003a; Klose et al., 2014). The default CLM5 uses the Zender et al. (2003a) scheme (hereafter Z03). Z03 is based on the Marticorena and Bergametti (1995) scheme and the White (1979) equation for saltation, which are used by many other global models (e.g., Foroutan et al., 2017; Meng et al., 2021; Klose et al., 2021; Wu et al., 2021). The Z03 dust emission equation has a form of:

$$F_d = S T C_{MB} \varphi f_{bare} \frac{\rho_a}{g} u_{*s}^3 \left(1 - \frac{u_{*t}^2}{u_{*s}^2}\right)\left(1 + \frac{u_{*t}}{u_{*s}}\right) \qquad \text{for } u_{*s} > u_{*t} \qquad (3)$$

where u_{*s} is the soil surface friction velocity (m s^{-1} ; $u_{*s} = u_*$ in Z03), F_d is the dust emission flux (kg m^2 s^{-1}), u_{*t} is the dust emission threshold (m s^{-1}; $u_{*t} = u_{*ft}$ in Z03), C_{MB} is a proportionality constant for bridging the gap between local-scale and large-scale dust emission fluxes, and φ is the sandblasting efficiency. S is the source function used to characterize the preferential source regions where fluvial sediment accumulates and to scale down the emission flux out of desert regions (Zender et al., 2003b). f_{bare} is the bare land fractional area; CLM5 uses a simple parameterization in which f_{bare} is a function of vegetation area index (VAI) defined as a sum of the leaf area index (LAI) and stem area index (SAI), so that dust emission scales down linearly with VAI and drops to zero when VAI > VAI$_{thr}$ (= 0.3; Mahowald et al., 2010; Kok et al., 2014b):

$$f_{bare} \propto (1 - f_v) \qquad (4)$$

where $f_v = $ VAI/VAI$_{thr}$ is the vegetation cover fraction. Other factors also considered to decrease bareness of the land such as the grid fraction of lake, snow cover, and the soil liquid content (see Oleson et al., 2013).

2.2 Atmospheric dust simulation

The land model (CLM5) simulates the dust emission as a function of soil and land properties (following Sect. 2.1), and the atmospheric model (CAM6) then takes the emission fluxes from the land model and simulates the transport, deposition, and microphysics (e.g., coagulation) of dust aerosols. The tropospheric modal aerosol model (MAM4) in CAM6 contains four aerosol modes (Liu et al., 2016): the Aitken mode (dust, sulfate, secondary organic matter, and sea salt), the accumulation mode (sulfate, secondary organic matter, primary organic matter, black carbon, sea salt, and dust), coarse mode (dust, sea salt, and sulfate), and the primary carbon mode (primary organic matter and black carbon). The size distribution of each mode is assumed to be log normal with fixed geometric standard deviations (GSDs) for each mode as 1.6 (Aitken), 1.6 (accumulation), 1.2 (coarse), and 1.6 (primary carbon). The geometric median diameters (GMDs) of the aerosol modes are then simulated accordingly. The emitted dust size distribution is derived from a parameterization based on brittle fragmentation theory (Kok, 2011) with the respective ratios of 0.1 %, 1.0 %, and 98.9 % for Aitken, accumulation, and coarse modes. Note that the coarse mode in CAM6 includes dust up to a diameter of ~10 μm and therefore misses the super-coarse dust ranged between 10 and 50 μm, and recent studies have therefore attempted to add more modes or particle bins to CAM (e.g., Ke et al., 2022; Meng et al., 2022). CAM6 then uses a tracer advection scheme to transport dust aerosols (Neale et al., 2012). Aerosols in each mode are transported as an internal mixture of the species present, with its physical properties (e.g., optical properties and density) predicted based upon the volume fraction of each species, while aerosol species from different modes are externally mixed. CAM6 simulates the removal of aerosols via dry deposition and wet deposition. Dry deposition includes turbulent and gravitational settling, as described in Zender et al. (2003a). Wet deposition includes in-cloud and below-cloud scavenging (Neale et al., 2012) of aerosols. The below-cloud precipitation provides rain and snow scavenging as a first-order process, which is the product of aerosol mass mixing ratio, precipitation flux, and scavenging coefficient (Dana and Hales, 1976). The in-cloud scavenging calculation assumes aerosols inside the cloud water are removed by precipitation, in proportion to the fraction of cloud water converted to rain through coalescence and accretion (Neale et al., 2012). The wet deposition rate depends on various factors including the prescribed dust hygroscopicity (0.068; Scanza et al., 2015) and the scavenging coefficient (0.1; Neale et al., 2012).

2.3 Coupled model configuration

The above dust emission equations are embedded into the CESM2.1 (hereafter CESM2; Danabasoglu et al., 2020), a coupled ESM with multiple earth system components including atmosphere, land, ocean, sea ice, etc. We use a component set (FHIST) of CESM2 that couples the land model component (CLM5) with the atmospheric component (CAM6), while other components (ocean, sea ice, glacier/land ice, etc.) are not active. The dust emission equations are simulated in CLM5. The meteorological and land surface variables that dust emission depends on, such as u_*, w, and ρ_a, are simulated by CLM5 and CAM6. The vegetation phenology in this configuration is prescribed from remote-sensing data (satellite phenology) in CLM5. We implement the new parameterizations described in Sect. 3 into CLM5 and evaluate the simulation performance with these new additional physics in Sect. 5. In the model configuration that we utilize in this study, atmospheric variables (e.g., wind and temperature) are simulated with a 30-minute timestep and are nudged every 3 hours toward the assimilated meteorology from the Modern Era Retrospective analysis for Research and Applications v2 (MERRA-2; Gelaro et al., 2017) obtained from the Global Modeling and Assimilation Office (GMAO). CAM6 has a default vertical resolution of 32 levels, and in this study, both CLM5 and CAM6 use a default horizontal resolution of 0.9°×1.25° with a default time step of 30 minutes. In this study, simulations are performed for 2003–2008 with 2003 discarded as a spinup year and 2004–2008 used for analysis purposes. We choose this time period because most of the observed and reanalysis datasets used for evaluation (described in Sect. 4) contain data over 2004–2008.

3 Modifications to the CESM2 dust emission scheme

In this section, we summarize the main improvements to the dust emission scheme proposed in Leung et al. (2022) and describe the new dust-related variables that these changes create.

3.1 A new physical dust emission equation

In this study, we replace the Z03 dust emission equation with a more physical dust emission equation from Kok et al. (2014b; hereafter K14) which has been adopted by a number of other global and regional models (Evan et al., 2015; Ito and Kok, 2017; Mailler et al., 2017; Li et al., 2021; Tai et al., 2021). One key difference between K14 and Z03 is that Z03 uses a spatial source function S to tune the dust emission flux to capture the magnitude of observed dust concentrations. S essentially quantifies the soil erodibility, defined as the efficiency of a soil in producing dust aerosols under a given wind stress (Zender et al., 2003b). The need for this source function indicates that Z03 is unable to capture the physical processes that determine soil erodibility across the globe. The largest difference between Z03 and K14 (and our scheme in Leung et al., 2022) is that Kok et al. (2014a) argued that soil erodibility (C_d in K14) can be directly related to soil aridity as characterized by the standardized fluid threshold $u_{*st} = u_{*ft}\sqrt{\rho_a/\rho_{a0}}$, because more erodible soils generally tend to have lower u_{*ft} and moisture values. u_{*st} is a pure function of moisture w since $\sqrt{\rho_a}$ cancels the $\rho_a^{-0.5}$ dependence in u_{*ft0} (from I&W82). Then the soil erodibility coefficient (or dust emission coefficient) in K14 is a pure function of u_{*st}:

$$C_d = C_{d0} \exp\left(-C_e \frac{u_{*st}-u_{*st0}}{u_{*st0}}\right) \tag{5a}$$

where C_{d0}, C_e, and u_{*st0} are constants. Following Kok et al. (2014b), the dust emission flux (kg m^{-2} s^{-1}) is:

$$F_d = \eta C_{tune} C_d f_{bare} f_{clay}' \frac{\rho_a(u_{*s}^2 - u_{*t}^2)}{u_{*st}} \left(\frac{u_{*s}}{u_{*t}}\right)^\kappa \qquad \text{for } u_{*s} > u_{*ft} \tag{5b}$$

Where u_{*s} is the soil surface friction velocity (= u_* in K14; to be detailed in Sect. 3.3), $u_{*t} = u_{*it} = u_{*ft}$ was assumed by K14 for simplicity, $\kappa = C_\kappa \frac{(u_{*st}-u_{*st0})}{u_{*st0}}$ is the fragmentation exponent quantifying the sensitivity of F_d to u_*, C_κ is a constant, C_{tune} is the global tuning factor for bridging the gap between local-scale and grid-scale dust emission fluxes (= 0.05 in CLM5), f_{clay}' is the soil clay fraction but capped at 0.2, and η is the intermittency factor (set as 1 in K14; to be detailed in Sect. 3.4). The biggest difference between Z03 and K14 is that the spatiotemporal variability of the K14 dust emissions is much more sensitive to the emission threshold u_{*ft} and the moisture w than Z03 (since, from Eq. 5a, C_d increases exponentially with u_{*st}). K14 showed improvements compared with Z03 when evaluated against ground-based dust AOD measurements (Kok et al., 2014b; Li et al., 2022). Same as Z03, VAI$_{thr}$ was set to be 0.3 in the K14 scheme. In the Leung et al. (2022) scheme, however, we set VAI$_{thr}$ = 1 mainly because observations show that there could be dust emitted from semiarid regions with VAI > 0.3 (e.g., Okin, 2008).

3.2 A revised dust emission threshold description

Based on the K14 scheme, the first proposed change by Leung et al. (2022) is to update a new representation of the effects of soil particle sizes to the modeling of the emission threshold. This includes simplifying the dust emission threshold parameterization and updating the soil particle diameter in the threshold scheme.

Following Leung et al. (2022), we first employ an alternative dust emission threshold scheme by Shao and Lu (2000; hereafter S&L00), which is derived from a more physical approach, is

280   computationally much simpler than I&W82, and produces a u_{*ft0} that is slightly more sensitive to D_p. S&L00 is given as:

$$u_{*ft0} = \sqrt{A(\rho_p g D_p + \gamma/D_p)}\, \rho_a^{-0.5} \qquad (6)$$

where $A = 0.0123$ and $\gamma = 1.65 \times 10^{-4}$ kg s^{-2} are empirical constants accounting for the magnitude of interparticle forces. S&L00 has a parabolic shape as a function of D_p, and $D_p \sim 80\ \mu$m corresponds to the

285   smallest u_{*ft0} of around 0.2 m s^{-1} (contingent upon the values of ρ_p, γ, and ρ_a). For larger sizes soil particles are heavier to lift; for smaller sizes soil particles are more strongly bound by interparticle forces. The S&L00 threshold scheme largely simplifies the I&W82 scheme by dropping the u_{*ft} dependence on the particle Reynold's number Re$_p$ and avoids the need of using an iterative method to calculate u_{*ft} (Oleson et al., 2013). We thus replace I&W82 with S&L00 in this study for CLM5 (following Leung et

290   al., 2022). u_{*ft} is then modeled following Eqs. 1–2. We set the tuning parameter for the moisture effect as $a = 2$ for our scheme to reduce the moisture effect on enhancing u_{*ft}, since it gives the best simulation results upon tuning.

      Then, we follow Leung et al. (2022) and employ a globally constant soil median diameter D_p of

295   127 μm for S&L00. Default CLM5 followed Zender et al. (2003a) and used a globally constant soil particle diameter of $D_p = 75\ \mu$m in I&W82, based on the argument that it is the optimal particle size that is the easiest to lift ($D_p = 75\ \mu$m corresponds to the smallest u$_{*ft0}$ in I&W82; see discussions in Kok et al., 2012). However, Martin and Kok (2019) showed that for mixed soils (i.e., soils with multiple sizes of soil particles mixed together), u_{*ft} should be a function of the median particle diameter of the soil PSD

300   instead of the optimal particle size that produces the smallest u_{*ft} possible. Leung et al. (2022) then used soil PSD observations from a suite of in-situ soil studies to show that the median D_p of the soil PSD measurements over arid regions were within a range of 40–250 μm. Regression analysis showed insignificant relationships between D_p and other soil textures and properties. Leung et al. (2022) showed that the D_p uncertainty range of 40–250 μm only translates to a u_{*ft0} range of 0.204–0.268 m s^{-1} using

305   S&L00, much smaller than the magnitude of u_{*ft} which goes beyond 1 m s^{-1}. Thus, Leung et al. (2022) argued it was reasonable to simplify and approximate the global median D_p by taking a mean across all the D_p observations, which was 127 μm. In this study, we introduce the use of $D_p = 127\ \mu$m as a global constant for the threshold schemes because it is conceptually more correct than using the optimal diameter of $D_p = 75\ \mu$m, although quantitatively it changes little the modeled u_{*ft}.

310

3.3 A wind drag partition scheme for reduced wind stress due to rocks and vegetation

      The second modification we proposed in Leung et al. (2022) is to include the effect of wind drag partitioning due to the presence of surface roughness elements, such as vegetation, rocks, pebbles, and

315   gravel, which protect the soil surface from wind erosion by absorbing part of the surface wind momentum. We account for the drag partitioning in the soil surface friction velocity u_{*s}:

$$u_{*s} = u_* F_{eff} \qquad (7)$$

where $F_{eff} \in [0,1]$ is the drag partition factor accounting for wind momentum absorption by surface roughness elements (rocks and plants). In the following, we describe the Leung et al. (2022) drag partition

320   scheme, which combines the effects of surface roughness due to rocks (Marticorena and Bergametti, 1995) and vegetation (Okin, 2008) to parameterize F_{eff}.

      Leung et al. (2022) and previous studies (e.g., Menut et al., 2013; Klose et al., 2021) used the aeolian roughness length z_{0a} to represent the roughness of rocks. z_{0a} represents small-scale

325 objects/obstacles of length scales of 1–10 m and is different from the typical aerodynamic momentum roughness length z_0 that represents the orography, terrain, and large-scale canopy roughness (Prigent et al., 2012; Menut et al., 2013). Leung et al. (2022) used the global aeolian z_{0a} dataset from Prigent et al. (2005) (hereafter Pr05), which contains the climatological z_{0a} (12 monthly values per grid) derived from the backscatter coefficient at 5.3 GHz measured by the European Remote Sensing (ERS) satellite. Because

330 z_{0a} quantifies the roughness of both rocks and vegetation, we take the minimum value out of 12 months for all grids to obtain an aeolian z_{0a} map to eliminate the effect of vegetation as much as possible. Furthermore, we apply this map over regions with VAI < 1, where the backscatter signal is mainly generated by rocks with lower contribution from vegetation roughness.

335 Marticorena and Bergametti (1995; hereafter M&B95) previously derived a parameterization to quantify the drag partition effect $f_{eff,r} \in [0,1]$ as a function of z_{0a}, which drops from one to zero as nonerodible roughness elements becomes more abundant over a surface (Darmenova et al., 2009):

$$f_{eff,r} = 1 - \frac{\ln\left(\frac{z_{0a}}{z_{0s}}\right)}{\ln\left[b_1\left(\frac{X}{z_{0s}}\right)^{b_2}\right]} \tag{8}$$

where $z_{0s} = 2D_p/30$ is the smooth roughness length, $X = 10$ m is a length scale set by Leung et al.

340 (2022), and $b_1 = 0.7$ and $b_2 = 0.8$ are empirical constants (Darmenova et al., 2009). We use the Pr05 global z_{0a} to obtain the rock drag partitioning $f_{eff,r}$, as shown in Fig. S1 for CLM5.

For vegetation drag partitioning, Leung et al. (2022) used the Okin (2008; hereafter O08) formulation, later simplified by (Pierre et al., 2014; hereafter P14) for GCMs, for modeling vegetation

345 drag partitioning as a single function of VAI. $f_{eff,v}$ that drops with increasing VAI:

$$f_{eff,v} = \frac{K + f_0 c}{K + c} \tag{9a}$$

$$K = 2\left(\frac{1}{f_v} - 1\right) \tag{9b}$$

where $f_{eff,v} \in [f_0, 1]$ is the area-averaged plant drag partitioning, K (dimensionless) is the normalized mean gap length between obstacles (plants), and $f_0 = 0.32$ and $c = 4.8$ are constants (Leung et al., 2022).

350 As the land gets more densely covered by vegetation, $K \to 0$ and $f_{eff,v} \to f_0$. The normalized mean gap length between obstacles K is a function of vegetation cover fraction $f_v = \text{VAI}/\text{VAI}_{thr}$ (Leung et al., 2022), which is more valid for small VAI (plants are further apart and do not overlap each other). We thus only apply this model over dust emission regions (VAI $\leq$ VAI$_{thr}$). VAI is thus the only input for Eq. 9. Using VAI (= LAI + SAI) that include both leaf and stem areas, this scheme is accounting for drag

355 partitioning due to both green and brown vegetation. Fig. S1b shows the resulting 2004–2008 mean global $f_{eff,v}$ map in CLM5.

After obtaining both the static $f_{eff,r}$ map for rocks and the time-varying $f_{eff,v}$ map for vegetation, we combine the two drag partition sources to capture and represent the total drag partition effect for dust

360 emission. Leung et al. (2022) obtained the fractions of a grid consisting of areas dominated by rocks and areas dominated by plants from the European Space Agency Climate Change Initiative (ESA CCI) dataset (ESA, 2017; https://www.esa-landcover-cci.org/?q=node/164, last access: 21 June 2022). The land cover product classifies the land cover of the whole globe into 37 categories (Li et al., 2018), with relevant land cover over arid regions such as shrub, herbaceous, sparse vegetation, cropland, grassland, as well as

365 consolidated (gravels and rocks) and unconsolidated (soil) bare land. Leung et al. (2022) formulated the hybrid drag partition factor F_{eff} for every grid given its fractional rock area A_r and fractional vegetation area A_v provided by ESA CCI:

$$F_{eff}^3 = A_r f_{eff,r}^3 + A_v f_{eff,v}^3 \tag{10}$$

where F_{eff} is simply the weighted mean of drag partition effects, and the exponent of three is the dust
emission exponent ($\kappa + 2$) of ~3 over deserts. An advantage of this weighted mean approach is that it
produces a very smooth transition of the drag partition effect from a rock-dominated regime (e.g., the
Sahara) to a plant-dominated regime (e.g., the Sahel), following the transition in land cover. We use Eq.
10 to obtain the global time-varying F_{eff}. Fig. 1a shows 2004–2008 mean of F_{eff} in CLM5, with more
grassy areas resembling $f_{eff,v}$ (e.g., the Southern Hemisphere, the U.S., the Tibetan Plateau, etc.) and
barer areas resembling $f_{eff,r}$ (e.g., the Dust Belt).

3.4 A dust emission intermittency scheme

Our third modification is to account for the effects of boundary-layer turbulent fluctuations on dust
emission intermittency. Dust emission intermittency exists because saltation is driven by high-frequency
turbulent surface winds (with frequencies of ~ 1 minute or less), which exhibit strong spatiotemporal
fluctuations in speed and direction. Instantaneous winds can thus pass within timescales much shorter than
a model time step (e.g., the CESM2 time step is about ~30 minutes with a ~100 km grid size) across both
u_{*ft} and u_{*it} for initiating or ceasing saltation (Martin and Kok, 2018). Consequently, saltation can be
highly intermittent (Comola et al., 2019), with pronounced variability in timescales of seconds to hours
(Dupont et al., 2013). However, existing dust emission parameterizations describe saltation as uniform in
time and space and driven by a constant downward momentum flux within a model time step (typically
30 minutes for CESM2). Neglecting intermittent dust emissions in current models thus likely degrades
the accuracy of dust emission simulations for arid regions during low-wind periods (when $u_{*s} < u_{*ft}$),
but especially for marginal dust source regions since u_{*ft} values are much greater than u_{*it} in high
moisture regions (using u_{*ft} to model dust will strongly underestimate dust emissions).

Since ESMs cannot explicitly resolve the high-frequency turbulent fluctuations, C19 employed
turbulent statistics to estimate the effect of high-frequency turbulent winds on generating dust emissions
within a time step. Here we briefly describe the C19 scheme that accounts for the intermittency effect on
dust emissions. C19 first formulates u_{*it} as a linear function of u_{*ft0} (Kok et al., 2012) from S&L00:

$$u_{*it} = B_{it} u_{*ft0} \tag{11}$$

where $B_{it} = 0.82$ is assumed to be a global constant. Dust emission intermittency happens when u_{*s} lies
between both thresholds ($u_{*it} < u_{*s} < u_{*ft}$). If u_{*s} within a model time step has a value between u_{*it}
and u_{*ft}, there will be small and fluctuating emission fluxes in reality, while LSMs using a u_{*ft} scheme
would predict zero emission within a model time step, thereby underestimating the emissions. Therefore,
it is important for climate models to employ u_{*it} instead of u_{*ft} in the dust emission equation. C19 thus
updates K14 by setting all u_{*t} terms in Eq. 5b as u_{*it} instead of u_{*ft}. Because $u_{*it} < u_{*ft}$, Eq. 5b
employing u_{*it} allows more small emission fluxes over the marginal source regions that are otherwise
missed by employing u_{*ft} as the threshold. Also, we follow Leung et al. (2022) to cap κ at 5 since a large
κ (e.g., > 10) combined with a small u_{*it} will occasionally produce unrealistically high emissions over
semiarid regions (which would not happen when using K14 with a large u_{*ft} over semiarid regions). The
intermittency factor $\eta \in [0,1]$ denotes the fraction of time that saltation and dust emission are active
within an ESM time step (e.g., 30 minutes for CESM2). C19 provided a parameterization of η using
information at the typical saltation height of z_{sal} (e.g., 0.1 m in C19), and η is formulated as a function of
the time-step (30-minutes) mean u_{*s}, u_{*it}, u_{*ft}, as well as the time-step standard deviation $\sigma_{\tilde{u}_s}$ of
instantaneous wind $\tilde{u}_s$ at $z_{sal} = 0.1$m (see Leung et al., 2022). η approaches one given $u_{*s} \gg u_{*ft}$,
approaches 0 given $u_{*s} \ll u_{*it}$, and values between zero and one when $u_{*it} < u_{*s} < u_{*ft}$ (intermittent
emission). The relationship between u_{*s} and η was portraited in Fig. 6a of Leung et al. (2022). Figure 1b

shows the 2004–2008 averaged intermittency factor η. Figures S2 shows the 2004–2008 averaged global
distribution of u_{*it}, u_{*ft}, and $u_{*ft}/u_{*it}(= f_m/B_{it})$ which scales with the moisture effect f_m.

3.5 An upscaling correction map for coarse-grid simulations

The final proposed modification in Leung et al. (2022) is to rescale the spatial variability of the
modeled dust emissions by a map of correction factors to account for the spatial variability of higher-
resolution dust emissions. Dust emission is a local-scale process with a typical length scale smaller than
1 km (Leung et al., 2022). ESMs with horizontal grid resolutions of ~100 km likely fail to capture locally
high emissions because the coarse meteorological and land surface fields used in the emission schemes
do not accurately represent the subgrid variability of dust emissions within a 100 km grid (Feng et al.,
2022). It is generally believed that the higher the horizontal resolution of an ESM, the better it simulates
the local spatial variability of emissions and captures the locally high emission peaks (Ridley et al., 2013).
Moreover, dust emission has nonlinear dependencies on multiple variables, especially u_{*s} ($F_d \propto$
$u_{*s}^{\kappa+2} \sim u_{*s}^3$ typically over deserts); as such, capturing the subgrid high wind peaks will result in more
emissions in a high-resolution simulation since the sensitivity $\partial F_d/\partial u_*$ is much stronger toward the higher
end of u_*. Thus, simulating dust in finer horizontal resolutions will generally result in higher global dust
emission fluxes (Ridley et al., 2013). Linearly interpolating those variables to calculate dust emissions
would be inaccurate as it is different from an area-weighted average of high-resolution dust emissions per
se (Ridley et al., 2013). Simply taking the area-weighted mean of high-resolution u_{*s} in a model grid box
will omit the locally high u_{*s} values that can produce locally extremely high emissions. There is a need
to better upscale low-resolution dust emissions to match the variability of high-resolution emissions, such
that dust emissions tend to be less resolution-dependent.

To mitigate the scale dependence of our dust emission simulations, we follow the approach in
Leung et al. (2022) to yield a map of scaling factors $\widetilde{K}_c$ for CESM2 that corrects the spatial variability of
the 0.9°×1.25° emissions $F_{d,c}$ to that of the 0.47°×0.62° emissions $F_{d,f}$. We conduct a 0.47°×0.62°
simulation and a 0.9°×1.25° simulation to yield a fine-resolution emission map $F_{d,f}$ and a coarse-
resolution emission map $F_{d,c}$. We normalize both emissions to have the same global total emission
(following Leung et al., 2022) to focus on the main differences in their spatial variability instead of their
magnitude differences. Then, dividing the annual $F_{d,f}$ map by the annual $F_{d,c}$ map for all grid cells results
in an annual scaling map $\widetilde{K}_c$ that accounts for the changes in the spatial variability of dust emissions
between high- and low-resolution simulations due to the subgrid variability of all meteorological and land
surface variables in the emission scheme:

$$\widetilde{K}_c(\text{lon}, \text{lat}) = F_{d,f}(\text{lon}, \text{lat})/F_{d,c}(\text{lon}, \text{lat}) \qquad (12)$$

where (lon, lat) indicate the longitude and latitude of each grid cell. $\widetilde{K}_c$ could then be multiplied by $F_{d,c}$
in CLM5 in the native 0.9°×1.25° simulation to adjust the spatial variability of $F_{d,c}$ to $F_{d,f}$ during the
native grid simulation, such that the subsequent dust cycle simulation in CAM6 can yield improved spatial
representation of dust variables such as DAOD.

The resulting annual $\widetilde{K}_c$ map in Fig. 1c shows the difference in spatial variability between the high-
and low-resolution emission simulations. The higher resolution run tends to produce more dust over the
semiarid and marginal source regions (red color), producing > 3–5 times more emissions than in the lower
resolution run. The reason is that lower-resolution runs employ coarse-resolution winds that smooth out
small-scale wind peaks, and marginal source regions have relatively high emission thresholds such that
the spatially averaged wind speed could easily be lower than the emission thresholds, leading to zero
emissions for the entire coarse grid. Therefore, low-resolution models will generally underestimate
emissions from marginal sources and create emission biases over hyperarid and other prominent source
regions. Since high-resolution simulations typically pick up more emissions from marginal sources, the

ratios over major sources (e.g., Sahara) are slightly smaller than 1 (light blue) as compensation to match the same global total emission.

Leung et al. (2022) suggested that modeled dust emissions should be multiplied by the $\widetilde{K}_c$ map to adjust the spatial variability of dust emissions and mitigate coarse model bias due to grid resolution. The degree of how much local-scale dust variability that the scaling map in Fig. 1c can capture is limited by the spatial resolutions and accuracies of the available input datasets, since some of the input fields (e.g., MERRA-2 meteorological fields) have a native horizontal resolution of ~ 0.5° that represents the highest local-scale variability of dust emissions the $\widetilde{K}_c$ map can capture. The emission increase over marginal sources may be even larger if the scaling factors were calculated using higher resolution inputs such as 0.25°×0.25° or finer (e.g., using ERA5 meteorology). In this paper, we adjust the spatial distribution of the CESM2 dust emissions by multiplying the 0.9°×1.25° dust emissions by $\widetilde{K}_c$.
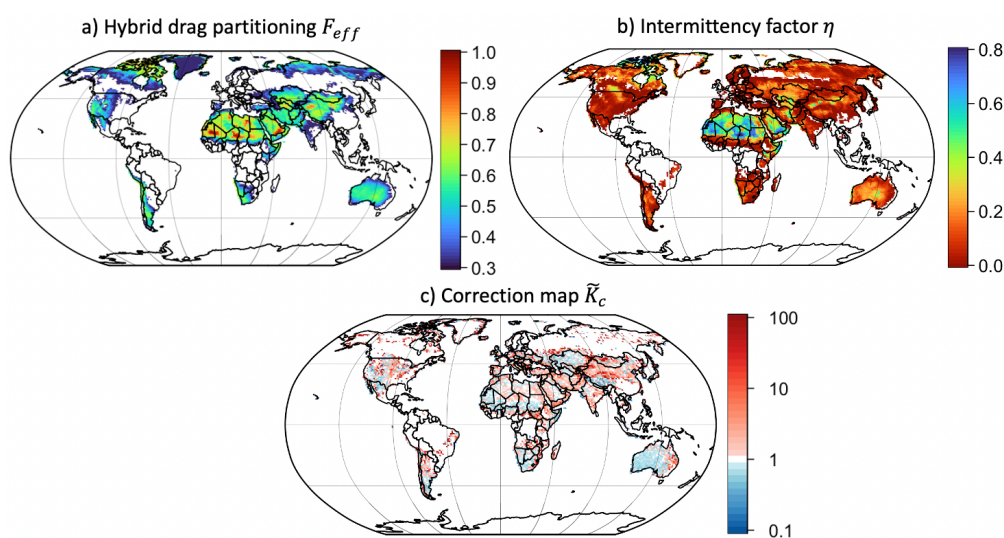

Figure 1. Implementations of proposed modifications in Leung et al. (2022) into the Community Land Model version 5 (CLM5). (a) Simulated hybrid drag partition effect F_{eff} on wind friction velocity considering the land surface roughness due to rocks and green vegetation. (b) The fraction of time that dust emission is active (intermittency factor η), averaging across all time steps when the emission flux $F_d > 0$. Note that the colorbar in (b) is inverted compared to (a) to show the contrasts in η between hyperarid and nonarid regions more clearly. (c) Correction map $\widetilde{K}_c$ for 0.9°×1.25° dust emission from the standalone dust emission model obtained in Leung et al. (2022).

4 observational and reanalysis datasets for evaluating the dust emission schemes

To evaluate the CESM dust cycle simulations using different dust schemes, we employ multiple observational and reanalysis datasets of atmospheric dust over various spatial scales for comparisons. This section briefly summarizes the independent datasets that we use to evaluate the CESM dust simulations.

4.1 Ridley et al. (2016) regional mean DAOD

We first employ a regional mean dust optical depth (DOD) dataset, constrained by Ridley et al. (2016) and compiled by Adebiyi et al. (2020) and Kok et al., (2021) (see Fig. 4 below). It is an observational–modeling constraint dataset on regional mean DAOD at 550 nm. Ridley et al. (2016) used various satellite AOD retrievals including the Multiangle Imaging Spectroradiometer (MISR) as well as

the Moderate Resolution Imaging Spectroradiometer (MODIS), all bias-corrected by the more accurate ground-based AOD measurements by the Aerosol Robotic Network (AERONET). They then obtained the
495 fraction of AOD due to dust using an ensemble of state-of-the-art global and region models, and combined the retrieved satellite AOD and the modeled dust fraction to total AOD to yield the DAOD. To reduce data uncertainties, Ridley et al. (2016) only chose 15 major dusty regions where dust contributed to a significant portion of total AOD (see Fig. S10 for the defined dusty regions) and obtained the regional mean DAOD instead of yielding grid-by-grid DAOD. Additionally, averaging across space and time
500 (2004–2008) enables error quantification of the regional mean DAOD. Nonetheless, Ridley's DAOD values over the Southern Hemisphere (SH) are subject to more biases than those over the Northern Hemisphere (NH), mainly because the dust fraction contributing to total AOD is much smaller over the SH. Following Kok et al., (2021), we thus instead use the regional mean DAOD values estimated by Adebiyi et al. (2020) that have smaller uncertainties over the three SH sources. Also, the regional mean
505 DAOD over North America was obtained from Adebiyi et al. (2020). This dataset represents seasonal DAOD values averaged over 2004–2008, and the values are presented in Table 2 of Kok et al. (2021). We will compare this dataset to our gridded DAOD simulations, averaged across years and grids to regional mean, for evaluation purposes.

510 **4.2 AERONET and AERONET–SDA AOD**
Additional observational dust properties are provided by the Aerosol Robotic Network (AERONET; Holben et al., 1998). For AOD, we consider the AOD v3 Direct Sun Algorithm level 2 (prefield and postfield calibrated, cloud-cleared, and manually inspected) data. We select 39 stations following Kok et al. (2014b) and Albani et al. (2014), based on the filtering criterion that only the dust-
515 dominant AERONET sites are picked (see Fig. S11 in Kok et al., 2014b for all selected sites). We further employ the AERONET coarse mode AOD data as retrieved by the spectral deconvolution algorithm (SDA; O'Neill et al., 2003), which was also used by other studies to represent DAOD (O'Neill et al., 2003; Capelle et al., 2018). Following Capelle et al. (2018), for some stations that do not contain level 2 data (not quality controlled and/or cloud-cleared), we use level 1.5 data for those sites instead. AERONET
520 takes multiple measurements within an hour during the daytime, with sub-hourly data available on the AERONET website. The website also compiles daily mean AOD data for the stations. We thus take the daily mean AERONET–SDA values, which are helpful for examining the spatiotemporal variability of the model simulations. The 2004–2008 mean AERONET–SDA coarse mode AOD values are shown in the upper panels of Fig. 5 as overlaid points.
525

4.3 MIDAS DAOD
In addition to the ground-based AOD observations, we also employ satellite AOD retrievals. A globally gridded reanalysis DAOD product was provided by Gkikas et al. (2021), namely the MODIS Dust Aerosol (MIDAS) dataset. MIDAS combines quality-filtered MODIS/Aqua AOD collection 6.1
530 level 2 at 550 nm with DAOD-to-AOD ratios from MERRA2 reanalysis to yield DAOD on the MODIS native grid. The resulting dataset has a fine spatial resolution of 0.1° × 0.1° and contains daily DAOD and AOD over 2003–2017. The uncertainties of the Aqua AOD and MERRA2 dust fraction are incorporated into the final MIDAS DAOD uncertainty. MIDAS DAOD highly complements AERONET AOD by providing global coverage of DAOD, with gridded AOD in high agreement with AERONET AOD (Fig.
535 3 of Gkikas et al., 2021). Another advantage of this dataset is that Gkikas et al. (2021) analyzed both land and ocean AOD, and thus MIDAS also provides DAOD over ocean surfaces. We will use the MIDAS dataset to examine the day-to-day variability of our gridded DAOD simulations. To match the horizontal resolution of CESM2, we regridded MIDAS DAOD from 0.1° × 0.1° to 0.9° × 1.25° (see Fig. 3d).

540 **4.4 In-situ PM concentration and deposition flux measurements**

We also use site measurements as climatological datasets for evaluating the spatial variability of dust PM and dust deposition simulations. Previous studies compiled dust PM measurements using high-volume filter collectors at the University of Miami Ocean Aerosol Network as well as station data that were previously compiled on annual averages (Mahowald et al., 2009; Zuidema et al., 2019). The dust

545   deposition flux climatology used here was compiled by Albani et al. (2014) and used in later studies (e.g., Li et al., 2022). Since CESM2 only simulated dust < 10 μm, Li et al. (2022) processed the data to estimate concentration and deposition only below the size cutoff using the reported parameters. The upper panels of Figs. 8–9 show the site dust PM$_{10}$ concentrations (μg m^{-3}) and dust deposition fluxes (kg m^{-2} yr^{-1}) as overlaid points.

550

5. Model evaluation

In this section, we evaluate the performance of the different dust emission schemes in CESM2: Z03, K14, and our scheme with more dust emission processes on top of K14, by comparing the spatial

555   and temporal variability of the modeled dust against observations and reanalysis datasets. We also discuss the effects of employing the scaling map $\widetilde{K}_c$ to rescale our scheme's emissions on the resulting dust cycle simulation.

We note that global dust simulations typically employ a global tuning factor that scales the global dust emission to a reasonable level that matches observations, since thus far there is no known *a priori*

560   physical principles that govern the order of magnitude of global total dust emission in the dust emission schemes. Past studies (e.g., Klose et al., 2021; Li et al., 2022) scaled the global dust emissions to produce a global mean modeled DAOD of ~0.03, which is a global constraint given by Ridley et al. (2016). In this section, we thus also scale our dust simulations with a global tuning factor in the CAM6 namelist variable (dust_emis_fact) like past studies (e.g., Li et al., 2022) did. However, we scale our emissions alternatively,

565   requiring the modeled DAOD to match Ridley's DAOD averaged across 15 dusty regions (of ~ 0.1) instead of averaged across the globe (see the 15 defined regions in Fig. S10, which is adapted from Table 2 of Kok et al., 2021). Here we require K14 and our scheme to be scaled such that the simulated DAOD mean across 15 dust regions are 0.1. Note that we do not scale the Z03 simulation since the default Z03 was already tuned by CESM2 modelers to optimize its performance.

570

5.1 CESM2 dust emissions using different emission schemes

Figure 2 shows the dust emissions that arise from Z03, K14, and the Leung et al. (2022) scheme

575   for 2004–2008. The spatial variability of the emissions for Z03 (Fig. 2a) is controlled by the geomorphic source function S developed by Zender et al. (2003b). S was a continuous function when formulated by Zender, but in CESM2 the source function is truncated for all values of S smaller than 0.1 (see Kok et al., 2014b; Li et al., 2022), resulting in a rather spatially discrete and disjointed pattern of emissions. It captures some major and marginal sources, such as the Bodélé Depression, the Taklamakan Desert,

580   Patagonia, the Karakum/Kyzylkum Deserts, and Australia. It does not fully capture some other major and secondary sources, such as the Rub' al Khali Desert over Saudi Arabia and deserts in the U.S. Several other regions like the Nubian Desert in Sudan/Egypt appear as prominent sources, which is not supported by satellite retrievals (Fig. 3d).

K14 emissions (Fig. 2b) show a much more continuous spatial pattern. The soil erodibility C_d

585   successfully captures emissions not only over major sources such as the Sahara and the Arabian Peninsula, but also emissions over semiarid regions and secondary sources such as the United States and central Asian deserts. Without the constraint of soil erodibility S in Z03, K14 produces much higher emissions over Australia because of the low moisture effect, and over the Horn of Africa (HoA) because of its very

high u_* compared to other hyperarid regions (see Fig. S3) especially during boreal summertime. In the
590   CESM2 simulation of K14, some major sources like the Taklamakan Desert have comparable or smaller
emissions than some semiarid regions such as the deserts in Australia, which could be a result of bias of
input meteorological fields or not including enough aeolian physics in the K14 parameterization.

Our scheme (Fig. 2c) adds extra aeolian physics on top of K14. While using D_p has little effect on
the spatial variability of the dust emission thresholds and the emission fluxes, the drag partition effect
595   F_{eff} modifies u_{*s} and highlights the major sources over the Bodélé Depression, El Djouf, and the Rub' al
Khali Desert. F_{eff} suppresses emissions from most semiarid regions with higher surface roughness, and
possibly oversuppresses emissions over semiarid areas, including the United States and the Thar Desert.
The intermittency effect increases emissions from remote regions such as the northern U.S., northern
Canada, and Siberia, and possibly overemphasizes emissions over the Tibetan Plateau.
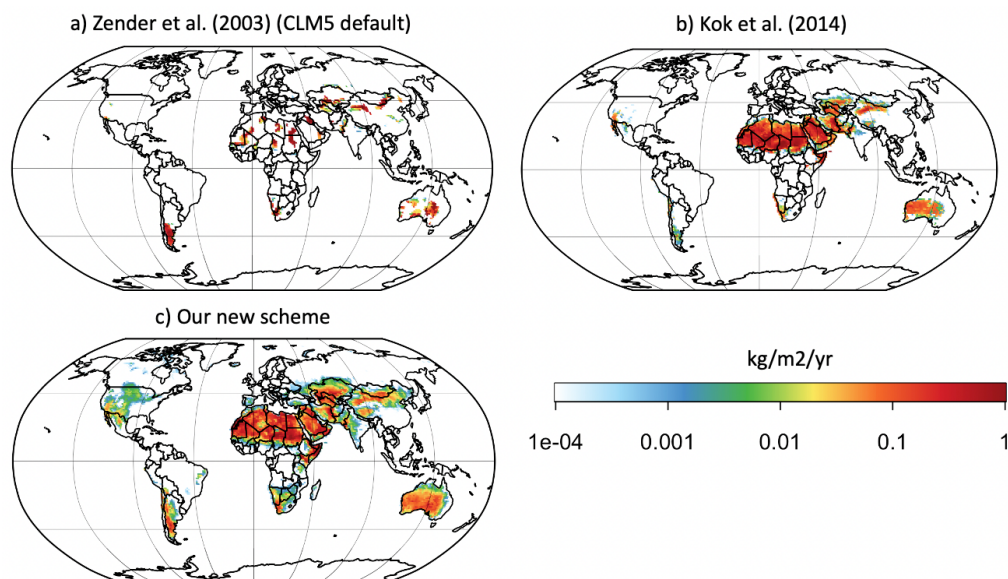
600

Figure 2. CESM dust emissions averaged across 2004–2008, for (a) Z03, (b) K14, and (c) our new
scheme (Leung et al., 2022).

605

5.2 DAOD spatial variability

Here we compare the spatial distributions of DAOD maps simulated by CAM6 using Z03 (Fig.
3a), K14 (Fig. 3b), and our scheme (Fig. 3c), as well as derived from MIDAS (Fig. 3d), averaged across
610   2004–2008. Figure 3d shows the MIDAS DAOD, with its peak over the Bodélé Depression of the Sahel
of ~ 0.6. DAOD is also moderately high over El Djouf and the southwestern Sahara (~0.3–0.4). The annual
MIDAS DAOD has several local peaks of > 0.3 (yellow color) over the Arabian Desert, the Thar Desert
in India, and the Taklamakan Desert over northwestern China. There are some modest DAOD levels over
central China, e.g., < 0.2 over the Sichuan Basin and the North China Plain (NCP), which are metropolitan
615   regions of high anthropogenic aerosol pollution (e.g., Leung et al., 2018). This indicates that MIDAS
might occasionally not be able to truncate all anthropogenic aerosol signals from the MODIS/Aqua AOD
data product.

Figure 3a shows the Z03 DAOD simulated by CAM6. The spatial pattern of Z03 DAOD in CAM6
is largely shaped by the Z03 source function (soil erodibility map S). It has multiple high DAOD regions

620   (> 1), including the Bodélé Depression, the Nubian Desert over Sudan, the eastern Arabian Peninsula, the Taklamakan Desert, the Strzelecki Desert in Australia, and some small peaks over southern Africa and South America. The DAOD values over these regions are all scaled up by the source function S and are unreasonably high compared with the MIDAS DAOD. The source function also generates DAOD peaks that are absent in observations, e.g., the Nubian Desert in Sudan.

625   Figure 3b shows the K14 DAOD simulated by CAM6. Without the source function, K14 has reduced DAOD over many source regions. K14 calculates the time-varying soil erodibility C_d, which indicates the most erodible region to be the Bodélé Depression, El Djouf, and the southern Sahara, resulting in the high DAOD ($\sim$ 0.6–0.7) over the south of Sahara. The western Sahel has a larger area of high DAOD (~0.6) over Mali/Niger, which is different from MIDAS that indicates a higher DAOD peak

630   over the Bodélé Depression than El Djouf. Due to the equatorial easterlies, dust advection toward the west leads to a DAOD 0.4–0.5 over a significant part of the tropical Atlantic Ocean. DAOD is also $\sim$ 0.3–0.4 over most of the Arabian Peninsula. Over Australia, the western region becomes the most erodible region because of low simulated soil moisture, which is not in agreement with observations which indicate the Strzelecki Desert (central Australia) has the highest DAOD.

635   Our new scheme's DAOD (Fig. 3c) shares a similar spatial variability with K14 DAOD. The main difference between K14 and our scheme's DAOD is the relatively lower DAOD levels over the Mali/Niger region where El Djouf is located because the drag partition effect reduces emissions over most of the Mali/Niger region (Fig. 3c). Figure S4 shows the difference between our scheme's DAOD and K14 DAOD. Comparing against MIDAS DAOD, our scheme and K14 overestimate dust over Australia and

640   the HoA. K14 and our scheme both overestimate DAOD over Sudan compared with the MIDAS DAOD because the dust emission equation is very sensitive to the low CESM soil moisture there, but our DAOD's high bias is smaller than K14 DAOD's. Both K14 and our scheme underestimate DAOD levels over the Taklamakan/Thar Deserts, which is also seen in other studies employing K14, e.g., Li et al. (2022) and Klose et al. (2021), likely because the high soil moisture levels in northwestern China suppress emissions.

645   None of the scheme captures the DAOD levels over the Thar Desert as shown by MIDAS. The overall improvements of our scheme's DAOD is that it better captures the DAOD values over El Djouf and reduces the DAOD overestimations over the Arabian Peninsula and Sudan. Our scheme also has higher DAOD levels over semiarid regions.
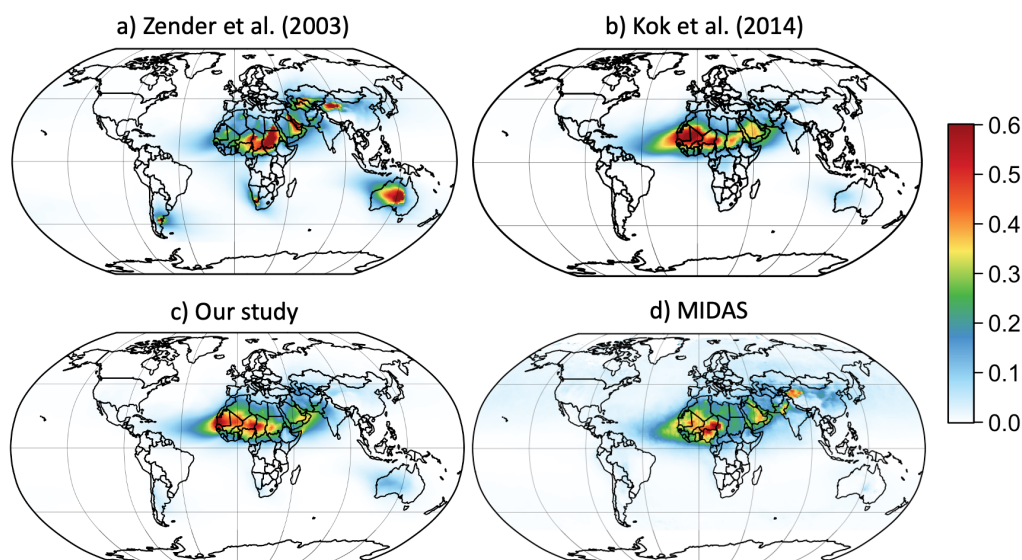

650

Figure 3. Global DAOD averaged across 2004–2008 from CESM2 and MIDAS. (a-c) CESM DAOD for (a) Z03, (b) K14, and (c) our new scheme (Leung et al., 2022). (d) MIDAS DAOD (Gkikas et al., 2021).

655   Next, we compare Ridley et al. (2016) regional mean DAOD with CAM6 simulated DAOD using Z03, K14, and our scheme in Fig. 4. Simulated regional DAOD are regionally averaged following the definition of 15 dusty regions (Fig. S10) in Kok et al. (2021). The upper and lower panels show the annual and seasonal mean regional DAOD, respectively. Our scheme's DAOD (Fig. 4c) shows the highest correlations with Ridley's DAOD (annual $R^2 = 0.82$; seasonal $R^2 = 0.76$), matching the regional DAOD distribution the best, whereas Z03 DAOD (Fig. 4a) produces the lowest correlations (annual $R^2 = 0.44$;

660   seasonal $R^2 = 0.42$) and the highest root-mean-square error (RMSE). Z03 overestimates annual DAOD over Bodélé/Sudan and Australia but underestimates DAOD over Mali/Niger and western Africa, which are primarily controlled by the strength of the source function S. K14 (Fig. 4b) shares a similar performance with our scheme matching against Ridley's regional DAOD values (annual $R^2 = 0.77$; seasonal $R^2 = 0.67$), but K14 overestimates the high regional DAOD values (e.g., Mali/Niger and

665   Bodélé/Sudan). K14 also tends to overestimate wintertime and springtime dust over the tropical Atlantic and western Africa. Both K14 and our scheme underestimate DAOD levels over the Taklamakan/Gobi Deserts and the Thar Desert (Figs. 4b and c), mostly due to underestimations of dust in the springtime (MAM; green color). Finally, MIDAS DAOD (Fig. 4d) has the highest consistency with Ridley's annual and seasonal mean DAOD (annual $R^2 = 0.96$; seasonal $R^2 = 0.95$).

670   Our new scheme has the reduced major axis (RMA) regression slopes the closest to the 1:1 line (annual slope = 0.92, seasonal slope = 0.82), demonstrating the smallest fitting bias among the three schemes. K14 DAOD has larger regional DAOD over Mali/Niger and El Djouf (Fig. 3b) and the RMA regression slopes moderately smaller than 1 (annual slope = 0.72, seasonal slope = 0.67). Z03 in CESM2 is pre-tuned, but also overestimates dust over major source regions (Fig. 3a) and the RMA slopes also

675   deviate from 1 (annual slope = 0.81, seasonal slope = 0.78). All three dust emission schemes (especially Z03 and K14) show systematic underestimations for lower regional DAOD values and overestimations for higher regional DAOD values, consistent with the findings of Zhao et al. (2022).

The reasons for the underestimations of lower regional DAOD values could be because the schemes are underestimating dust emissions from marginal source regions (with lower regional DAOD

680   values). It could be further because ESMs overestimate wet depositions of dust over tropical oceans (Albani et al., 2014; van der Does et al., 2020), for possible reasons including an overestimated light rain frequency (Wang et al., 2021) and a higher hygroscopicity due to internal mixing with other aerosols (Neale et al., 2012). ESMs also overestimate dry depositions for reasons that remain unclear but could include turbulence in dusty layers and an underestimation of the extent to which particle asphericity

685   enhances drag (Weinzierl et al., 2017; Huang et al., 2020; Meng et al., 2022; Drakaki et al., 2022). These factors all contribute to a shorter lifetime of dust, enhancing the dust concentration contrasts between sources and downwind / far-field regions.
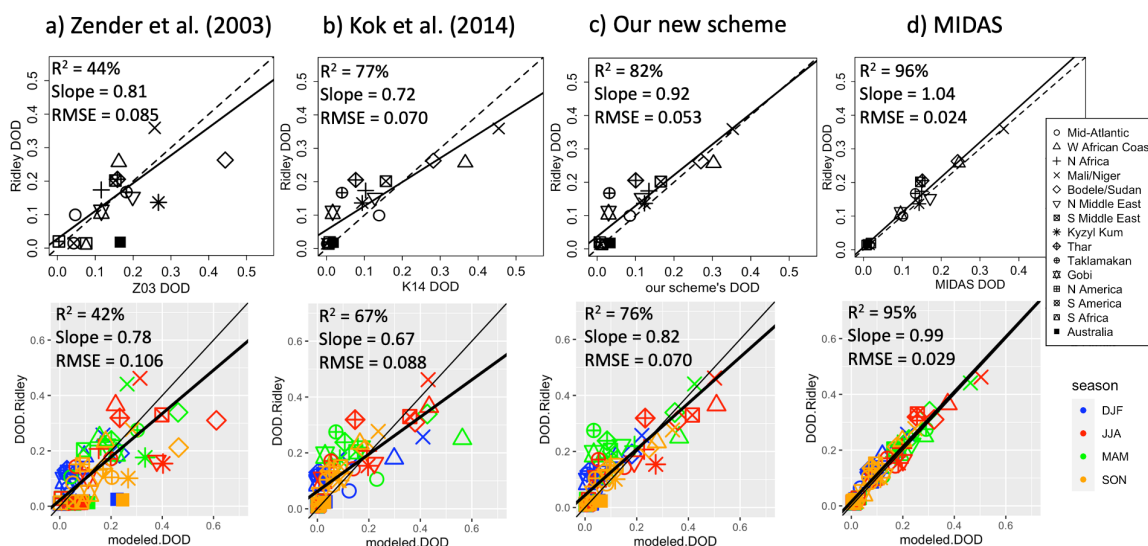
Figure 4. Ridley et al. (2016) regional mean DAOD vs. modeled CESM2 DAOD using (a) Z03, (b) K14, and (c) our scheme, as well as (d) MIDAS DAOD (Gkikas et al., 2021), for 2004–2008 over 15 dusty regions (see Fig. S10) defined following Kok et al. (2021). Top panels show annual mean DAOD scatterplots, with dashed lines as 1:1 lines and solid lines as the reduced major axis (RMA) regression lines. Bottom panels show seasonal mean DAOD scatterplots for the three schemes, with thin lines as 1:1 lines and thick lines as the RMA regression lines. Seasons are defined as: DJF (December–January–February), MAM (March–April–May), JJA (June–July–August), and SON (September–October–November).

Next, we evaluate the simulated spatial DAOD variability against coarse mode AOD observations at multiple AERONET stations. Figure 5 compares the satellite-derived MIDAS DAOD and the CESM2 simulations against the AERONET–SDA coarse mode AOD. The 39 site locations we chose (Sect. 4.2) are over arid regions such that the coarse mode aerosols are mostly dust. MIDAS (Figs. 5d and h) gives the best agreement when compared against AERONET, yielding the largest coefficient of determination (R^2) of 0.76 and the smallest RMSE of 0.065. RMA regression gives a slope of 1.11 (blue line), which is close to the 1:1 line (black line).

Evaluating the dust emission schemes using the AERONET AOD measurements gives the similar conclusion as using the Ridley DAOD values. The Z03 scheme (Fig. 5a and e) shows the lowest degree of agreement against AERONET with an RMSE of 0.21, more than three times the RMSE of MIDAS DAOD. Z03 substantially overestimates DAOD over Australia (Fig. 5a) because of the large source function S there (AOD values are < 0.1 for the Australian AERONET sites). There are also multiple underestimations of Z03 DAOD of ~0.3 over the Sahel, which can be > 0.5 for AERONET sites (Fig. 5a). Note that although Z03 has a relatively decent regional RMA regression slope in Fig. 4a, Z03 shows much stronger bias against AERONET AOD with an RMA slope of 0.66 because it strongly overestimates DAOD over hyperarid regions. Meanwhile, K14 (Figs. 5b and f) yields a much higher spatial R^2 of 0.70 and a much smaller RMSE of 0.080 against AERONET data. K14 has fewer DAOD underestimations over the Sahara–Sahel region and reduced DAOD overestimations in the Arabian Peninsula and Australia (Fig. 5f). The RMA regression slope of 0.85 shows that K14 simulates the spatial variability of AERONET AOD relatively well compared to Z03, different from Fig. 4b which shows that K14 regionally has stronger seasonal DAOD bias than Z03. This suggests that evaluating dust schemes against regional and

17

720   local station data can yield different conclusions regarding biases. Our new scheme (Figs. 5c and g) reduces the bias generated by K14, yielding an RMA regression slope of 1.02. Our scheme's DAOD yields an R^2 of 0.73 and an RMSE of 0.072, marking modest improvements over K14 simulations. Overall, our scheme performs the best among three schemes in capturing the spatial AOD variability of AERONET sites.

725
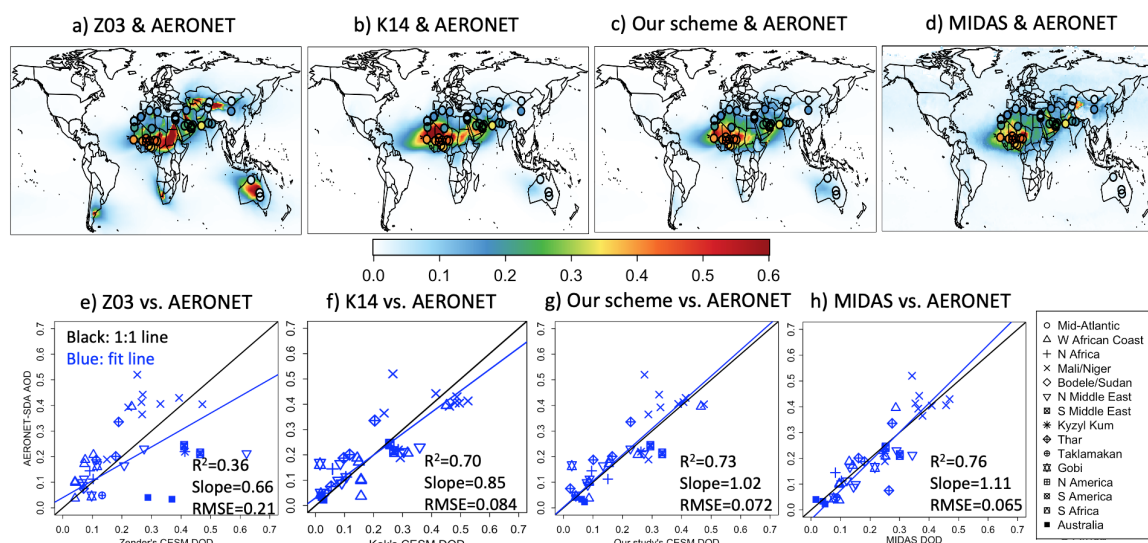
Figure 5. Gridded model/satellite DAOD vs AERONET–SDA coarse mode AOD for 2004–2008. Top panels show the global dust AOD for (a) MIDAS (b) Z03, (c) K14, and (d) our scheme, overlaid by
730   AERONET sites of coarse mode AOD observations. (e–h) The respective scatterplots for AERONET AOD versus (e) MIDAS DAOD, as well as CESM DAOD using (f) Z03, (g) K14, and (h) our scheme.

5.3 DAOD day-to-day variability

735

        Apart from examining the spatial variability, we also examine the temporal variability of CESM2 dust using different dust emission schemes. Here we use globally gridded daily MIDAS DAOD across 2004–2008 and multiple stations of AERONET–SDA coarse mode daily AOD for evaluations. For MIDAS DAOD, we calculate grid-by-grid daily Pearson correlations between MIDAS and CESM2
740   DAOD, yielding a global correlation map for each scheme (Fig. 6). Here we focus on showing and discussing the correlation results over regions with MIDAS DAOD/AOD fraction > 0.25 only. Gridboxes with MIDAS DAOD/AOD < 0.25 are smoothed and masked out because the MIDAS DAOD time series over those regions contain little dust signal and are less credible. Figure S6 shows the grid-by-grid correlations of Fig. 6 without any masking, and Fig. S7 shows the MIDAS global DAOD/AOD fraction
745   for 2004–2008. also further discuss the daily correlations of dust with the driving meteorological and land surface variables at the end of this subsection (see also Figs. S8 and S9).
        In Fig. 6a, Z03 dust shows overall strong daily correlations with MIDAS dust over the Dust Belt and the tropical Atlantic. The correlations are generally lower over the eastern than the western Sahara, likely partially due to the strong extra dust sources represented by Z03 over Sudan/Egypt, which is absent
750   in MIDAS DAOD. The predominant easterly trade winds bring dust signals from Sudan to the central and western Sahara, likely reducing correlations over dust sources such as the Bodélé Depression. Another

possible reason is because the daily correlations between Z03 dust and the driving meteorological fields over the eastern Sahara are generally modest, with R of only ~ 0.1–0.2 (see Figs. S8a-c). Another region of strong correlations occurs over the Arabian Sea, indicated in Fig. 6a as dominated by dust from the HoA, meaning both MIDAS and Z03 agree that dust advects from the HoA to central Asia and regulates dust air quality in downwind regions. Z03 also shows high correlations with MIDAS over the Thar Desert and moderately high correlations over China, especially over the Taklamakan Desert. This partially indicates that although the regional emission strengths of Z03 are likely overestimated as shown in the previous subsection, the Z03 source mask indeed helps emphasize the true source origins of dust, which subsequently benefit a more accurate temporal dust variability over the Taklamakan and its downwind regions.

K14 dust in Fig. 6b generally shows weaker correlations with MIDAS dust over the Dust Belt than the other two schemes. K14 has smaller correlations with MIDAS than Z03 (negative ΔR values in Fig. 6d), despite the fact that K14 emission has stronger daily correlations with the driving fields than Z03 dust (Figs. S8d-f). One possible reason is that K14 emissions over most of the Sahara are similarly strong (Fig. 2b), meaning K14 is less capable of distinguishing primary emission sources from secondary sources. As a result, simulated dust signals over downwind regions (western Africa and the Atlantic) could be contaminated by dust signals from secondary sources such as Sudan, Western Sahara, and western Mauritania. The same issue likely occurs over the eastern Sahara since the Arabian Peninsula (upwind of the eastern Sahara) emits similar orders of magnitude of dust across most of the Peninsula instead of coming primarily from the Rub' al Khali Desert. Correlations over the Taklamakan Desert also appear weaker than in Z03 (Fig. 6d), possibly because of the higher-than-observed dust emissions from the Karakum/Kyzylkum region in central Asia advected by the predominant westerlies that contaminate dust signals over the Taklamakan.

Our scheme in Fig. 6c captures similar correlations as Z03 overall, with higher correlations (R ~ 0.7–0.8) over western Africa, the Atlantic, the Arabian Sea, and India. Our scheme performs modestly better than Z03 over the northern Sahara (the Algerian Desert and the Libyan Desert) as well as the Sahel and the Gulf of Guinea (positive ΔR values in Fig. 6e), which is likely a result of dust coming from more correct source regions. Modestly better performance is also seen over the Rub' al Khali Desert likely due to the wind drag partition corrections. Additionally, our scheme's dust emission correlates better with meteorological drivers than K14 and Z03 (Fig. S8g-i), especially with u_{*s}, which likely also helps improve the DAOD correlations with MIDAS DAOD. Meanwhile, a more significant reduction in correlations occurs over China when comparing with Z03 (Fig. 6e). The correlations over the Taklamakan are lower than Z03 likely because our scheme's emissions in the Taklamakan are too low, such that the DAOD over the Taklamakan have mixed DAOD signals from the Karakum/Kyzylkum region. Similarly, our scheme also produces lower dust correlations downwind of the Gobi Desert. The Gobi probably should emit less dust than the Taklamakan Desert to generate a reasonable day-to-day DAOD variability over the Gobi. An inverse modeling study by Wang et al. (2012) also indicated that during dust events, modeled Gobi emissions were optimized to be about 20 % of Taklamakan emissions to match the observed MODIS AOD record. Figs. 6d-f also support the conclusion that schemes (e.g., Z03) that successfully generates more Taklamakan emissions than Gobi emissions (e.g., Fig. 2a) could yield better dust temporal correlations against MIDAS over northern China than schemes (e.g., K14 and our scheme; Figs. 2b and c) that produce similar levels of emissions from both deserts. There are some additional moderate correlation differences over central China (negative $|\Delta R|$ values in Fig. 6e), which are metropolitan regions with vast anthropogenic aerosols (e.g., Leung et al., 2018). This again indicates that, as discussed in Fig. 3d, MIDAS DAOD might still contain some anthropogenic aerosol signals in urban regions.
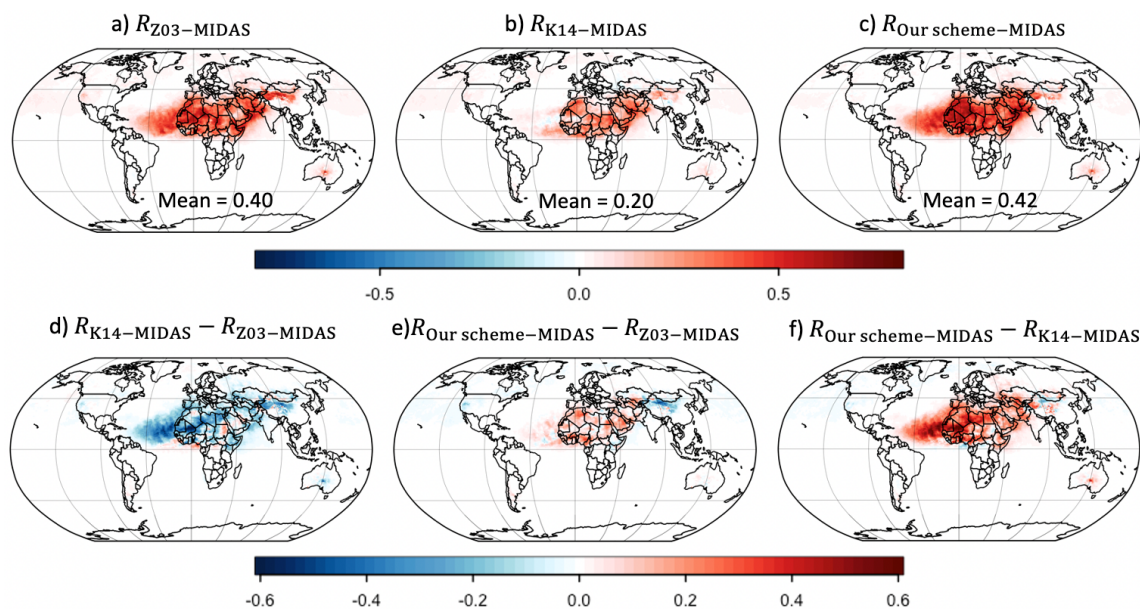
Figure 6. Grid-by-grid MIDAS DAOD daily Pearson correlation maps with CESM2 DAOD for 2004–
2008. (a-c) Correlation maps R of MIDAS daily DAOD time series vs. CESM2 daily DAOD time series
using (a) Z03, (b) K14, and (c) our scheme. The correlation maps focus on gridboxes with MIDAS
DAOD/AOD ratio > 0.25 only. Pixels with MIDAS DAOD/AOD < 0.25 are filtered and smoothed out.
Figure S6 shows the unfiltered correlation maps. The values at the bottom of the panels show the global
mean correlation values (for all gridboxes with MIDAS DAOD/AOD > 0.25). (d-f) Changes (ΔR) in
correlation maps from (d) Z03 to K14, (e) Z03 to our scheme, and from (f) K14 to our scheme.

For AERONET data, we calculate daily Pearson correlations between the selected AERONET
stations and the CESM2 grids that contain those stations. The conclusions are similar to the ones discussed
in Fig. 6. For Z03 (Fig. 7a), strong correlations are generally seen over the Sahara and central Asia because
of a relatively decent representation of the locations of dust sources. Z03 has a generally weaker
representation of the temporal dust variability over Australia, as in K14 and our scheme. For K14 (Fig.
7b), the correlations over the Sahara tend to be weaker (R around 0–0.4), likely due to the inadequate
representation of dust source locations. The sites over northern and eastern Australia yield smaller
correlations in K14 than Z03, because the modeled dust signals over there are contaminated by emissions
from the west, which has higher emissions than the east. Our scheme yields overall the highest correlations
across the globe out of all schemes. Our scheme's dust highly correlates with MIDAS dust over the Sahara
and the Middle East ($R \sim 0.5$–0.8). Correlations over the Australian sites in our scheme are also the highest
among all schemes ($R \sim 0.3$–0.5), even though our scheme generates similar orders of magnitude of
emissions across different parts of Australia (in Fig. 2c). One issue is the correlation over a Mongolian
site to the north of the Gobi is about zero (the weakened correlation also occurs in the K14 simulation in
Fig. 7b). As discussed in the previous paragraph, this is likely a result of our scheme's inability to generate
high dust emissions from the Taklamakan than the Gobi, such that the DAOD signal over the Mongolian
site is contaminated by the dust from other sources. Meanwhile, Z03 with high Taklamakan emissions and
low Gobi emissions yields a high R of ~ 0.6 over the Mongolian site.
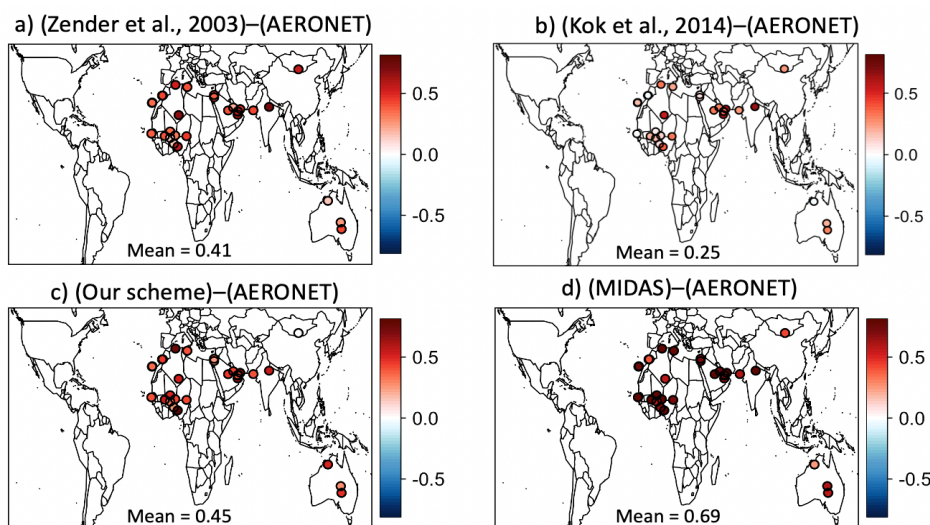
20

Figure 7. AERONET–SDA coarse mode AOD daily correlations for 2004–2008 over selected sites with CESM DAOD using (a) Z03, (b) K14, and (c) our study. (d) MIDAS DAOD versus AERONET–SDA AOD daily correlation. The values at the bottom of the panels represent the mean correlation across all AERONET stations.

As discussed above, our scheme's dust not only matches well with external dust datasets but also correlates better with meteorological drivers in day-to-day variability than Z03 and K14 (in Figs. S8 and S9), for a number of reasons. First, implementing more aeolian physics (Sect. 3) allows our scheme to better couple with the simulated boundary-layer dynamics, vegetation dynamics, and the water cycle in CESM2. For example, our scheme's emission strongly covariates with u_{*s} (Fig. S8g) since the emission's dependence on u_{*s} is not only in the K14 dust emission equation (Eq. 5) but also in the C19 intermittency scheme (Sect. 3.4), resulting in an enhanced sensitivity of emissions to the winds. Another example is that our emission's dependence on VAI is not only in the bare land fraction term (Eq. 4) but also in the vegetation drag partitioning (Eq. 9), enhancing the dust correlation with VAI (Fig. S8h and Fig. S9h). The second reason is because the use of u_{*it} in the dust emission equation increases the likelihood of emission $F_d > 0$ in the F_d time series. Z03 and K14 employing u_{*ft} have a lot of times with emission $F_d = 0$ in the time series, weakening their emissions' temporal variability and thus the covariation with u_{*s}. With more pronounced temporal fluctuations, our scheme's F_d is further sensitive to the variability of u_{*s} and correlate better with other driving variables than Z03 and K14. Third, the implemented aeolian processes allow more coupling between the driving fields such as boundary-layer meteorology and vegetation dynamics. For instance, as VAI regulates u_{*s} through the vegetation drag partition effect, u_{*s} carries both the temporal variability of u_* and VAI. u_{*s} thus almost dictates the temporal behavior of the our scheme's emission time series analogous to the concept of dimensionality reduction ($R \sim 1$ in the Sahara; Fig. S8g). Figures S8 and S9 show that our scheme's emission and DAOD are very sensitive to the day-to-day variability of meteorological and land surface variables, which means our scheme is likely also more sensitive to climate change and land use and land cover change (LULCC) in longer-term simulations.

5.4 Comparisons against other measurements of the dust cycle

We use more datasets of different dust cycle variables from other independent sources to evaluate our CESM2 dust cycle simulations regarding spatial variability. Figure 8 compares the simulated dust
860   PM_{10} concentrations using various schemes versus observed dust PM from multiple stations. Z03 has some strong overestimations compared with the measurements over the downwind regions of dust sources (dark red in the bottom panel of Fig. 8a), such as over Japan, southern Australia, and South Africa. Dust concentrations over the source regions are very high (e.g., the Taklamakan desert and the Australian desert in the top panel of Fig. 8a), partially due to the emphasis by the Z03 source mask. Our scheme in Fig. 8c
865   reduces the exaggerations of dust strength in Z03 over Asia, Australia, and other secondary sources, mitigating the overestimations of dust PM as shown in the bottom panel of Fig. 8c compared to Fig. 8a. Our scheme mainly overestimates dust PM over the Sahara, which is commonly shared by Z03 and K14 and consistent with the previous discussion on regional DAOD (Zhao et al., 2022). Due to in the insufficient emissions over the Taklamakan, our scheme produces ~60 μg m^{-3} of dust PM there, smaller
870   than the ~100 μg m^{-3} reported by other observational studies (e.g., van Donkelaar et al., 2016; Leung et al., 2018; van Donkelaar et al., 2021). Our scheme produces higher dust PM than K14 (Fig. 8b) over arid and semiarid regions, including the Gobi, the United States, and Patagonia. Compared with Z03's spatial correlation of $R = 0.80$ (in the $\log_{10}$ space), our scheme yields a slight increase in the spatial correlation of $R = 0.90$. Overall, dust PM concentrations tend to be underestimated over the downwind regions (e.g., the
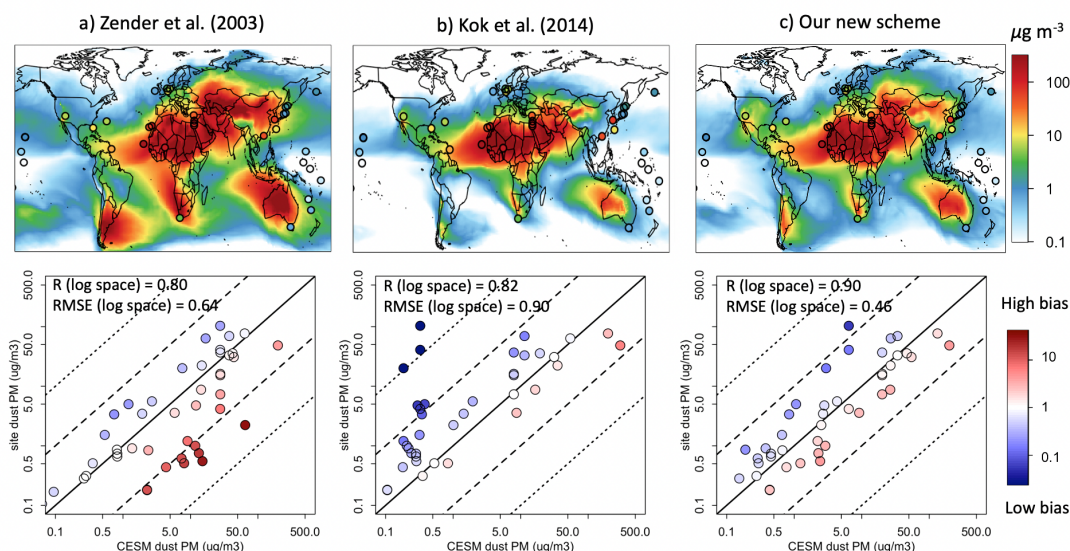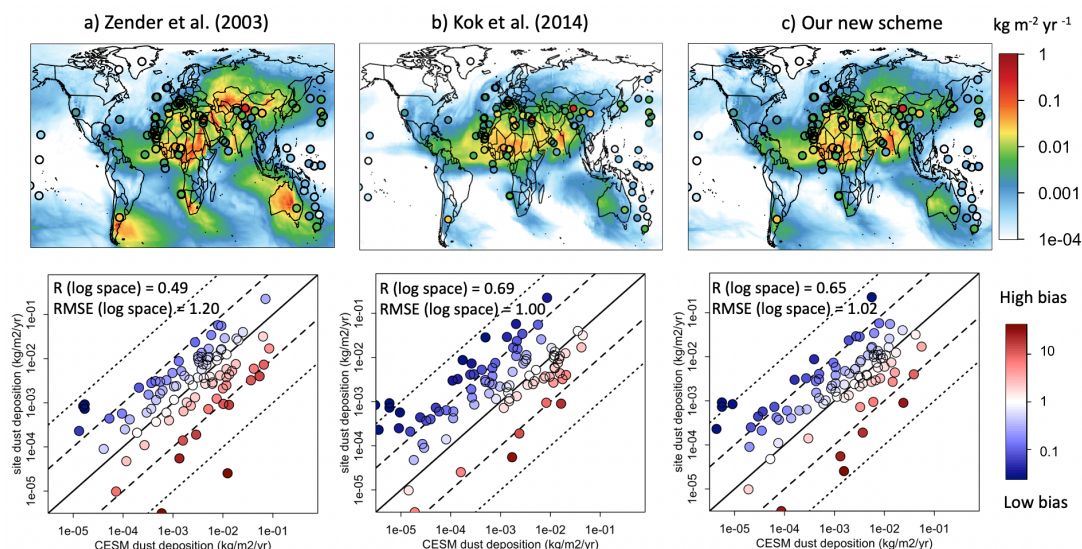875   Pacific and the Atlantic).

Figure 8. CESM2 dust PM_{10} concentration (in μg m^{-3}) vs. climatological in-situ PM_{10} measurements (Sect. 4.4) for (a) Z03, (b) K14, and (c) our study. The color bar in the bottom panels indicates the degree of
880   overestimation (red) and underestimation (blue) of the simulated dust PM compared with in-situ PM measurements.

Figure 9 shows the dust deposition evaluation for all schemes. All schemes show that most deposition fluxes are concentrated over the source regions. Over remote areas (e.g., the central Pacific
885   Ocean and the Southern Ocean), simulated deposition fluxes are small with an order of magnitude of ~10^{-4} kg m^{-2} yr^{-1} or smaller (white color), whereas measurements over those locations generally have an order of magnitude of 10^{-4} (light blue). It shows that the deposition schemes in CAM6 are problematic in that dust typically deposits too quickly; switching between dust emission schemes does not address nor mitigate the issue. Generally, the spatial patterns of dust depositions follow those of the DAOD

890 (comparing Fig. 3 with Fig. 9). Our scheme has a higher correlation of $R = 0.65$ (in the log space) compared with $R = 0.49$ by Z03, but K14 has an even slightly higher $R = 0.69$. There are some underestimations of dust depositions over the downwind regions of Asia (i.e., the extratropical Pacific) but some overestimations of depositions over the downwind regions of the Sahara (i.e., the equatorial Atlantic). The results indicate that there is likely an overestimated tropical wet scavenging of dust, consistent with
895 findings from previous studies (e.g., Albani et al., 2014; van der Does et al., 2020).

Figure 9. CESM dust total (dry + wet) deposition (in kg m^{-2} yr^{-1}) vs. climatological in-situ deposition measurements for (a) Z03, (b) K14, and (c) our study. The color bar in the bottom panels indicates the
900 degree of overestimation (red) and underestimation (blue) of the simulated dust PM compared with in-situ PM measurements.

5.5 Effects of employing a scaling map to correct dust emission

905

In this subsection, we discuss the effects on the simulated dust cycle in CAM6 of using a correction map ($\widetilde{K}_c$) to scale our scheme's dust emissions simulated in the native 0.9°×1.25° resolution to be consistent with 0.47°×0.62° emissions of our scheme (Sect. 3.5). We focus on the changes in the DAOD spatial variability; changes in other dust cycle variables are shown in Fig. S5. Figure 10a shows the global
910 DAOD of our scheme after correction, which is not visibly very distinct from the uncorrected DAOD in Fig. 3c. Figure 10b shows the ratio between the corrected DAOD and the uncorrected DAOD, both normalized to the same global mean, to better visualize their spatial variability discrepancies. It is worth comparing the map of DAOD discrepancies (Fig. 10b) to the map of emission discrepancies (Fig. 1c). The more prominent sources, e.g., the Sahara, have suppressed DAOD compared to other dusty regions ($\widetilde{K}_c \sim$
915 0.8–0.9; light blue in Fig. 10b). This is because, as discussed in Fig. 1c, high-resolution simulations produce more emissions from semiarid regions than low-resolution simulations but produce similar emission levels from primary sources as low-resolution simulations, leading to a relative suppression of dust over primary sources upon scaling to the same global mean DAOD. Many secondary dust sources have relatively enhanced dust levels, most noticeably the two American regions ($\widetilde{K}_c \sim$ 1.2–1.8), but the
920 absolute increases in DAOD are modest as the baseline DAOD levels over there are low. The Taklamakan/Gobi region also has a moderate rise in DAOD ($\widetilde{K}_c \sim 1.3$).

Since the high-resolution simulations generally pick up more emissions over semiarid regions, $\widetilde{K}_c$ tends to reduce the DAOD regional biases seen in Fig. 4 by enhancing the underestimated DAOD over semiarid regions and suppressing the overestimated DAOD over major sources. Comparing against the Ridley et al. (2016) regional DAOD (Figures 10c-d), northern Africa has reduced DAOD and southern hemispheric regions have increased DAOD, hence slightly enhancing R^2 slightly from 0.82 to 0.84 and annual RMSE to drop from 0.053 to 0.048. Annual RMA regression slope modestly changes from 0.92 (in Fig. 4c) to 0.94. This shows that $\widetilde{K}_c$ helps reduce the biases of annual and regional mean DAOD predictions. However, since the errors mainly originate from seasonal biases, the improvements of using an annual $\widetilde{K}_c$ map are relatively modest. For instance, in Fig. 10d, the significantly underestimated MAM DAOD (in red) in Asia and the Middle East are still not resolved by using the annual $\widetilde{K}_c$. Using a seasonal or monthly $\widetilde{K}_c$ would more effectively reduce seasonal DAOD biases.

Although the correction map modestly improves the regional variability of DAOD, it does not necessarily produce improvements in comparisons against site-level dust observations. Figure 10e compares AERONET–SDA coarse mode AOD with the corrected DAOD of our scheme. Although the scatterplot has an increased RMA slope from 0.97 (in Fig. 5h) to 0.99, the R^2 value drops from 0.71 to 0.65 and the RMSE increases from 0.077 to 0.088. This is mainly due to the small DAOD underestimations over major sources like Mali/Niger and Bodélé/Sudan (see the "x" points). Our rescaled simulation has a reduced Mali/Niger DAOD that better matches Ridley's regional DAOD; however, it loses its local DAOD peaks and matches less well against AERONET–SDA AOD. There are also DAOD overestimations over the southern Middle East. This evaluation likely has a bias in geographical location because the errors are mainly from major sources; if more selected AERONET stations were in the Taklamakan/Gobi and the U.S., this evaluation against AERONET would possibly show better results because our rescaling reduces the DAOD underestimations over those regions. Overall, this evaluation shows that despite the better performance in capturing the regional DAOD variability using $\widetilde{K}_c$, it does not necessarily guarantee a better performance in the grid-scale or site-scale spatial DAOD variability .

Finally, Fig. 10f shows that the annual $\widetilde{K}_c$ has few effects on the temporal variability of DAOD simulations, which depicts the correlation map differences ΔR between our scheme's rescaled DAOD versus MIDAS DAOD ($R_{\mathrm{corrected}}$) and our scheme's uncorrected DAOD versus MIDAS DAOD ($R_{\mathrm{uncorrected}}$ from Fig. 6c). ΔR values are statistically insignificant across the globe (Sect. S1). It is reasonable that $\widetilde{K}_c$ changes little our scheme's DAOD temporal variability because $\widetilde{K}_c$ is a time-invariant map here that is meant to only change the spatial variability of the simulated dust.
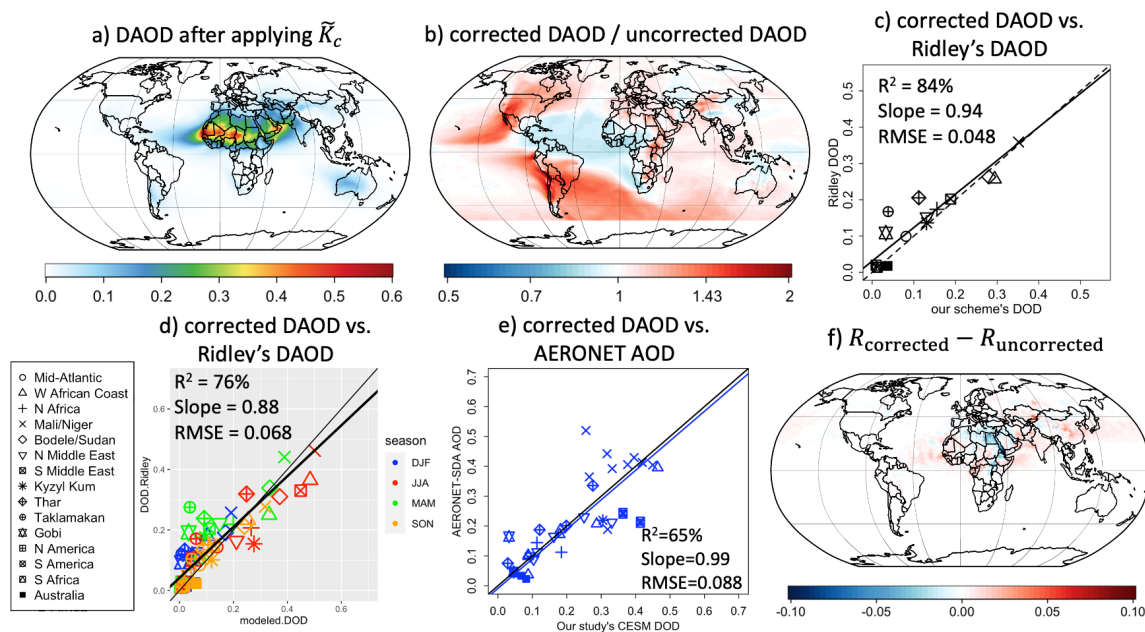
Figure 10. Effects of using the scaling map $\widetilde{K}_c$ to correct the 0.9°×1.25° CLM5 dust emissions on the CAM6 dust cycle. (a) DAOD spatial pattern simulated by our scheme after the global dust emission pattern is corrected by $\widetilde{K}_c$. (b) Corrected DAOD (Fig. 10a) divided by the uncorrected DAOD (Fig. 3c). Both DAOD maps are rescaled to have the same global mean to emphasize their difference in spatial variability. (c, d) Corrected DAOD versus Ridley regional DAOD (c) annually and (d) seasonally. (e) Corrected DAOD versus AERONET–SDA coarse mode AOD. (f) Changes in correlation maps (ΔR) between corrected DAOD vs. MIDAS DAOD and uncorrected DAOD vs. MIDAS DAOD.

6. Discussion and Conclusions

This study has evaluated the new formulation of the dust emission scheme proposed in Leung et al. (2022) against measurements and compared its performance against existing emission schemes in CESM2. The major modifications implemented into CESM2 are the following: 1) updating the soil median particle diameter (as an input parameter to the dust emission threshold calculation) from 75 μm as proposed by Zender et al., (2003a) to 127 μm; 2) including a parameterization for the drag partition effect that accounts for the impact of not only rocks but also green and brown vegetation on reducing the wind stress available for soil erosion; 3) implementing the intermittent dust emission parameterization by Comola et al. (2019) that accounts for the effects of boundary-layer turbulence on dust emissions, and 4) rescaling the CESM2-native resolution dust emissions toward high-resolution emissions. Following Leung et al. (2022), these modifications are 5) implemented on a newer dust emission parameterization of Kok et al. (2014b; K14) instead of the default Zender et al. (2003a, b; Z03) scheme in CLM5, although the modifications 1–4 can also be implemented on top of Z03 or any other emission scheme. The major advances of Leung et al. (2022) are mainly that the drag partition effect successfully moves emissions toward important dust sources (e.g., the Bodélé Depression and El Djouf) and thus generates a more realistic spatial distribution of dust than Z03 or K14. Also, the intermittency scheme generates more emissions from semiarid regions and even high-latitude regions, in agreement with observations.

25

Our new scheme showed improvements over previous schemes (Z03 and K14) in terms of both the spatial and temporal variability of dust cycle variables. For instance, our scheme showed improved agreement against the annual and seasonal regional DAOD quantified by Ridley et al. (2016). Indeed, our scheme's annual regional DAOD had an R^2 of 0.82 and RMSE of 0.053, compared to Z03's R^2 of 0.44 and RMSE of 0.080. Evaluating against the AERONET–SDA coarse mode AOD, our scheme's DAOD yielded an R^2 of 0.71 and RMSE of 0.077 compared to Z03's R^2 of 0.36 and RMSE of 0.15. Our scheme also generated improved spatial distributions of dust PM_{10} concentrations and depositions against site measurements of PM_{10} and deposition fluxes than Z03 (Figs. 8 and 9). For day-to-day temporal variability, our scheme's DAOD also matched the MIDAS DAOD better over most of the Dust Belt than Z03 DAOD (Fig. 6e), with larger correlations of on average $\Delta R \sim 0.15$ (p-value < 0.05; Sect. S1). Our scheme's DAOD also showed high daily correlation values (with a mean of 0.45) against AERONET–SDA daily AOD time series (Fig. 7). However, our scheme's DAOD generally showed worse performance in representing the day-to-day dust variability over East Asia (Fig. 6e and Fig. 7c), likely because of the significant low bias of dust (DAOD $\sim$ 0.1) over the Taklamakan Desert such that dust over East Asia was dominated by other transboundary dust signals instead of dust from the Taklamakan. Generally, our scheme better represented the spatial variability of Ridley's regional DAOD, the site-level AERONET DAOD, the site-level dust PM, as well as the day-to-day temporal variability of MIDAS DAOD than the default Z03 scheme. Our scheme's dust also shows better correlations with driving meteorological and land surface variables (e.g., u_{*s}, VAI, w; Figs. S8 and S9), and is thus likely more sensitive to climate change and LULCC than other emission schemes' dust. Since the more physically based Leung et al. (2022) scheme showed improvements in the model–observation comparison (Sect. 5), the developments in Leung et al. (2022) will be introduced into a future CLM (and CESM) version for the benefit and use of the dust community and the CESM community.

Regardless of which dust emission scheme is used, Fig. 4 shows that CESM2 tends to overestimate DAOD over major sources (e.g., the Sahara) and underestimate DAOD over marginal source regions (e.g., SH sources) and downwind regions (e.g., oceans). This result is consistent with previous findings across multiple ESMs (Zhao et al., 2022), likely due to the low dust emission thresholds (low gravimetric soil moisture) over the hyperarid regions compared with those over the semiarid regions. Theoretically, employing the intermittency scheme helps generate more emissions from semiarid regions, thereby reducing the DAOD biases and increasing the RMA slopes toward one. Our scheme did yield RMA slopes that most closely match the 1:1 line among all emission schemes (annual RMA slope = 0.92).

We then tested the proposed modification of rescaling dust emissions of lower resolutions toward higher resolutions by Leung et al. (2022). We used the 0.9°×1.25° and 0.47°×0.62° simulations from CESM2 to construct an annual correction map $\widetilde{K}_c$ (Eq. 12) used to rescale and correct the CESM2-native 0.9°×1.25° dust emissions to the spatial variability of the finer resolution (0.47°×0.62°) emissions. Employing the scaling map $\widetilde{K}_c$ further reduced the CESM DAOD over hyperarid regions and enhanced DAOD over secondary sources. Figs. 10c–d showed that correcting the CESM2-native 0.9°×1.25° dust emissions increased the R^2 and reduced the RMSE of the CESM DAOD against the Ridley et al. (2016) regional DAOD. As shown in Fig. 10b, the higher DAOD values over semiarid regions (e.g., North and South America) tilted the RMA slope (= 0.94) further closer to the 1:1 line. Similar to the unscaled simulation of our scheme (Fig. 4c), the more significant DAOD errors after rescaling still came from the underestimation of the DAOD in the Taklamakan, the Gobi, and the Thar (Fig. 10c). Since $\widetilde{K}_c$ is a time-invariant map, employing $\widetilde{K}_c$ has little effects on improving the seasonal / day-to-day variability of the CESM DAOD (Figs. 10d and f). In summary, employing an annual $\widetilde{K}_c$ to dust emissions modestly improved the spatial variability of atmospheric dust but altered little its temporal variability. This modification differs from other modifications proposed by Leung et al. (2022) in that it does not

necessarily improve the process representation of the dust scheme, but the methodology makes the scheme more scale-aware and consistent toward high-resolution dust simulations. Without $\widetilde{K}_c$, our new process-based emission scheme will still work in ESMs across different resolutions and in regionally refined models (RRMs).

1035

Although CESM2 with our updated dust emission scheme thus shows an improved spatiotemporal pattern of DAOD, some important biases remain. Our scheme's dust overestimations include DAOD levels over the Horn of Africa (HoA) and Australia, as well as over the Taklamakan. The DAOD hotspot over the HoA (in Fig. 3c) is due mainly to the very high u_* in MERRA-2 nudged CESM2 (> 0.5 m s^{-1} in

1040 Fig. S3), resulting in a high dust emission flux of ~ 1–2 kg m^{-2} yr^{-1} (Fig. 2c) that is almost as high as emissions over the Bodélé Depression. The unrealistically high emissions from the HoA produce a dust plume extending to the Middle East (e.g., Oman), central Asia, and as far as the Thar Desert due to the downwind transport. This problem also occurs in the default K14 and Z03 schemes (Figs. 2a-b), although Z03 uses a source mask that significantly reduces the HoA emissions. As for Australia, the relatively low

1045 soil moisture over the central and western parts of the country results in somewhat higher emissions in western than eastern Australia. Our study therefore shows a modest annual DAOD peak of ~0.2 (Fig. 3c) over western Australia (e.g., the Great Sandy Desert and the Gibson Desert), which is different from the smaller eastern peak of ~0.1 in MIDAS/Aqua DAOD (Fig. 3d). In addition, CESM2 shows an annual DAOD of only ~0.1 over the Taklamakan/Gobi region in China, which is a strong underestimation

1050 compared with the yearly DAOD of ~0.35 from MIDAS/Aqua. This DAOD low bias occurs because CESM2 simulates over there a low emission flux (Fig. 2c) as a result of the moderately high soil moisture w and aeolian roughness length z_{0a} (compared with the Sahara). Furthermore, CESM background dust levels over downwind regions (e.g., the tropical Atlantic and the extratropical Pacific) are generally underestimated compared with MIDAS DAOD, likely because of the strong dust depositions and short

1055 lifetimes of dust, leading to dust preferentially depositing over the land.

Although we have attempted to improve the dust emission model in both CLM5 and CAM6, there are more areas of dust cycle modeling that warrant further developments. We summarize several main issues in dust modeling that should be addressed in future versions of CESM and other ESMs to further

1060 enhance the dust modeling performance in the land and atmospheric models:

1. Dust emission physics: There are several mechanisms that affect the dust emission threshold that are not currently accounted for in most dust emission modules. First, soil crusts due to soil microbes can strongly aggregate soil particles and prevent winds from eroding the soils

1065 (Rodriguez-Caballero et al., 2018). Second, the impact of anthropogenic activities, such as agriculture/tillage, on dust emission is not explicitly included in dust emission modules, although new parameterizations for anthropogenic dust emissions are under development (e.g., Xia et al., 2022). Third, apart from saltation bombardment, soil particles can enter the atmosphere through direct aerodynamic entrainment (Klose and Shao, 2012). Models have been developed to represent

1070 direct particle entrainment into the atmosphere (Klose and Shao, 2013; Klose et al., 2014).

2. Dust size distribution: Apart from dust emission physics, there are problems in representing the dust aerosol size distributions in the atmosphere. Coarse and super-coarse dust particles are substantially underestimated (Adebiyi and Kok, 2020), and recent studies are working on implementing the coarse and super-coarse dust size bins (CAM4; Meng et al., 2022) or modes (Ke

1075 et al., 2021; CAM5) in different versions of CAM, such that CESM2 can represent the impacts of large dust particles on climate and ecosystem. Recent studies further found that the geometric standard deviations (GSDs) of the accumulation and coarse modes in CAM6 are too narrow (Wu

et al., 2020; Li et al., 2022), which subsequently adversely impacted the dust deposition, lifetime, and size distribution of the CAM6 simulations.

1080
   3. Dust deposition: Dust deposition in ESMs is generally overestimated, and dust lifetime is underestimated (e.g., Albani et al., 2014; van der Does et al., 2020; Huang et al., 2021) due to a few reasons. First, recent studies found that dust particles are highly aspherical, which subsequently alters the aerodynamic resistance of dust and slows down the dry deposition velocity of dust (Huang et al., 2021). This finding increases the lifetime of coarser dust particles and also

1085
       reduces the mass extinction efficiency (Huang et al., 2023). This effect of dust asphericity on dry deposition and extinction is being implemented into climate models (e.g., Klose et al., 2021; Li et al., 2022; Meng et al., 2022). Second, the default dry deposition scheme in CAM6 (Zhang et al., 2001) is known to overestimate dry deposition of fine dust, and Li et al. (2022) has employed a newer dust deposition scheme (Petroff and Zhang, 2010) to resolve the issue. Third, the modal

1090
       aerosol model (MAM) of CESM2 merges dust and other aerosols (e.g., sea salt) into the same modes (e.g., accumulation and coarse modes) with internal mixing, such that the wet deposition of dust is likely overestimated (e.g., the Atlantic Ocean) due to the higher hygroscopicities of other aqueous aerosols (Neale et al., 2012). Fourth, studies reported that modeled dust depositions are too high over the tropical oceans (Albani et al., 2014; van der Does et al., 2020).

1095
   4. Speciation of dust: CESM and other ESMs mostly parameterize dust as a single mineral (e.g., aluminum silicate; Emmons et al., 2020), which cannot adequately represent a suite of chemical reactions, radiative effects, and cloud processes that depend on mineralogy. Recent studies have initiated the modeling of multiple dust species (e.g., haematite, quartz, illite, feldspar, calcite) and better represented the dust optical properties and radiative effects (Li et al., 2021, 2022; Gonçalves

1100
       Ageitos et al., 2023). Emergence of satellite measurements of global soil mineralogy such as from the Earth Surface Mineral Dust Source Investigation (EMIT; Green et al., 2020; Thompson et al., 2020) mission under NASA will help better represent dust species from specific source regions.

   5. Chemistry and cloud processing: A correct mineralogical representation of dust is essential for representing the role of dust in atmospheric chemistry and aerosol–cloud interactions. Previous

1105
       studies have documented multiple chemical reaction pathways via which dust interacts with tracer gases and aerosols (Gaston, 2020; Adebiyi et al., 2023; Kok et al., 2023). Dust acts as a source or sink of multiple chemical species, such as oxidants (e.g., ozone), aerosol precursors (e.g., sulfur dioxide and nitric acid), aerosols (e.g., via coagulation), halogens (e.g., chlorine), and more (Tang et al., 2017; Mitroo et al., 2019; Gaston, 2020). Furthermore, although many ESMs include the

1110
       impacts of dust on ice cloud formation (Storelvmo, 2017), dust seeding on warm cloud formation are quantified in only a few ESMs (e.g., McGraw et al., 2020) as dust is considered hydrophobic by many ESMs. Chemical dust aging is crucial for dust to gain hygroscopicity and become effective cloud condensation nuclei (CCN). A comprehensive mineralogical representation of dust and a more complex heterogeneous dust chemistry are required to adequately represent the roles

1115
       of dust in the formation of warm, ice, and mixed phase clouds, as well as the effects of dust–cloud interactions on indirect radiative effects and forcings in ESMs.

       Finally, while many dust modeling studies focused on improving and evaluating the spatial representation of modeled dust, the importance of evaluating the temporal variability of modeled dust is

1120
likely undervalued. Relatively few dust studies (e.g., Zhang et al., 2013; Klose et al., 2021; LeGrand et al., 2023) provide evaluation of the temporal changes in dust emissions and DAOD. This study represents one of the early attempts to conduct a global-scale evaluation of the day-to-day variability (Figs. 6–7) of the simulated dust time series (along with studies like Klose et al., 2021). The next step in improving dust modeling should be on enhancing the long-term (interannual or interdecadal) variability of dust, especially

1125
since recent studies (e.g., Kok et al., 2023) found that ESM dust trends do not reproduce the historical increasing trends of dust. It is highly warranted to investigate how transient climate change and LULCC

regulate the long-term variability of observed dust and reproduce them in ESMs. Improving long-term ESM dust predictions will also benefit the study of the epidemiological consequences of future dust changes on human health, risk management, and mitigation strategies (Philip et al., 2017; Achakulwisut et al., 2019; Bauer et al., 2019; van Donkelaar et al., 2021).

1130

Author Contributions

J. F. K. and D. M. Leung conceptualized the study. D. M. Leung performed the model development, conducted the simulations, analyzed the simulation results, and conducted the evaluations. D. M. Leung

1150 wrote the original manuscript and plotted all figures under J. F. K.'s supervision. L. Li, C. P. G.-P. M. K., S. T., D. M. Lawrence, N. M. M., and E. K. assisted the conceptualization and model development. All authors contributed to the manuscript preparation, discussion, and writing.

Competing Interests

1155 The authors declare no competing interests.

Data and Code Availability

The MODIS Dust Aerosol (MIDAS) daily dust aerosol optical depth data from Gkikas et al. (2021) are available at https://zenodo.org/record/4244106#.ZEbR7OzMIlI. The satellite-derived aeolian roughness

1160 data are available upon contacting Catherine Prigent. The in-situ dust PM and dust deposition measurements are available upon contacting Natalie M. Mahowald. ESA CCI land cover can be obtained from https://www.esa-landcover-cci.org/?q=node/164. The CESM2 code for the new dust emission scheme is available at https://github.com/ESCOMP/CTSM/pull/1712/files.

1165

References

Achakulwisut, P., Anenberg, S. C., Neumann, J. E., Penn, S. L., Weiss, N., Crimmins, A., Fann, N., Martinich, J., Roman, H., and Mickley, L. J.: Effects of Increasing Aridity on Ambient Dust and

1170   Public Health in the U.S. Southwest Under Climate Change, GeoHealth, 3, 127–144, https://doi.org/10.1029/2019GH000187, 2019.

Adebiyi, A., Kok, J. F., Murray, B. J., Ryder, C. L., Stuut, J.-B. W., Kahn, R. A., Knippertz, P., Formenti, P., Mahowald, N. M., Pérez García-Pando, C., Klose, M., Ansmann, A., Samset, B. H., Ito, A., Balkanski, Y., Di Biagio, C., Romanias, M. N., Huang, Y., and Meng, J.: A review of

1175   coarse mineral dust in the Earth system, Aeolian Research, 60, 100849, https://doi.org/10.1016/j.aeolia.2022.100849, 2023.

Adebiyi, A. A. and Kok, J. F.: Climate models miss most of the coarse dust in the atmosphere, Science Advances, 6, eaaz9507, https://doi.org/10.1126/sciadv.aaz9507, 2020.

Adebiyi, A. A., Kok, J. F., Wang, Y., Ito, A., Ridley, D. A., Nabat, P., and Zhao, C.: Dust Constraints

1180   from joint Observational-Modelling-experiMental analysis (DustCOMM): comparison with

measurements and model simulations, Atmos. Chem. Phys., 20, 829–863, https://doi.org/10.5194/acp-20-829-2020, 2020.

Albani, S., Mahowald, N. M., Perry, A. T., Scanza, R. A., Zender, C. S., Heavens, N. G., Maggi, V., Kok, J. F., and Otto-Bliesner, B. L.: Improved dust representation in the Community Atmosphere Model, Journal of Advances in Modeling Earth Systems, 6, 541–570, https://doi.org/10.1002/2013MS000279, 2014.

Bauer, S. E., Im, U., Mezuman, K., and Gao, C. Y.: Desert Dust, Industrialization, and Agricultural Fires: Health Impacts of Outdoor Air Pollution in Africa, Journal of Geophysical Research: Atmospheres, 124, 4104–4120, https://doi.org/10.1029/2018JD029336, 2019.

Capelle, V., Chédin, A., Pondrom, M., Crevoisier, C., Armante, R., Crepeau, L., and Scott, N. A.: Infrared dust aerosol optical depth retrieved daily from IASI and comparison with AERONET over the period 2007–2016, Remote Sensing of Environment, 206, 15–32, https://doi.org/10.1016/j.rse.2017.12.008, 2018.

Comola, F., Kok, J. F., Chamecki, M., and Martin, R. L.: The Intermittency of Wind-Driven Sand Transport, Geophysical Research Letters, 46, 13430–13440, https://doi.org/10.1029/2019GL085739, 2019.

Dana, M. T. and Hales, J. M.: Statistical aspects of the washout of polydisperse aerosols, Atmospheric Environment (1967), 10, 45–50, https://doi.org/10.1016/0004-6981(76)90258-4, 1976.

Danabasoglu, G., Lamarque, J.-F., Bacmeister, J., Bailey, D. A., DuVivier, A. K., Edwards, J., Emmons, L. K., Fasullo, J., Garcia, R., Gettelman, A., Hannay, C., Holland, M. M., Large, W. G., Lauritzen, P. H., Lawrence, D. M., Lenaerts, J. T. M., Lindsay, K., Lipscomb, W. H., Mills, M. J., Neale, R., Oleson, K. W., Otto-Bliesner, B., Phillips, A. S., Sacks, W., Tilmes, S., van Kampenhout, L., Vertenstein, M., Bertini, A., Dennis, J., Deser, C., Fischer, C., Fox-Kemper, B., Kay, J. E., Kinnison, D., Kushner, P. J., Larson, V. E., Long, M. C., Mickelson, S., Moore, J. K., Nienhouse, E., Polvani, L., Rasch, P. J., and Strand, W. G.: The Community Earth System Model Version 2 (CESM2), Journal of Advances in Modeling Earth Systems, 12, e2019MS001916, https://doi.org/10.1029/2019MS001916, 2020.

Darmenova, K., Sokolik, I. N., Shao, Y., Marticorena, B., and Bergametti, G.: Development of a physically based dust emission module within the Weather Research and Forecasting (WRF) model: Assessment of dust emission parameterizations and input parameters for source regions in Central and East Asia, Journal of Geophysical Research: Atmospheres, 114, https://doi.org/10.1029/2008JD011236, 2009.

Di Biagio, C., Balkanski, Y., Albani, S., Boucher, O., and Formenti, P.: Direct Radiative Effect by Mineral Dust Aerosols Constrained by New Microphysical and Spectral Optical Data, Geophysical Research Letters, 47, e2019GL086186, https://doi.org/10.1029/2019GL086186, 2020.

van der Does, M., Brummer, G.-J. A., Crimpen, F. C. J. van, Korte, L. F., Mahowald, N. M., Merkel, U., Yu, H., Zuidema, P., and Stuut, J.-B. W.: Tropical Rains Controlling Deposition of Saharan Dust Across the North Atlantic Ocean, Geophysical Research Letters, 47, e2019GL086867, https://doi.org/10.1029/2019GL086867, 2020.

van Donkelaar, A., Martin, R. V., Brauer, M., Hsu, N. C., Kahn, R. A., Levy, R. C., Lyapustin, A., Sayer, A. M., and Winker, D. M.: Global Estimates of Fine Particulate Matter using a Combined Geophysical-Statistical Method with Information from Satellites, Models, and Monitors, Environ. Sci. Technol., 50, 3762–3772, https://doi.org/10.1021/acs.est.5b05833, 2016.

van Donkelaar, A., Hammer, M. S., Bindle, L., Brauer, M., Brook, J. R., Garay, M. J., Hsu, N. C., Kalashnikova, O. V., Kahn, R. A., Lee, C., Levy, R. C., Lyapustin, A., Sayer, A. M., and Martin, R. V.: Monthly Global Estimates of Fine Particulate Matter and Their Uncertainty, Environ. Sci. Technol., 55, 15287–15300, https://doi.org/10.1021/acs.est.1c05309, 2021.

Drakaki, E., Amiridis, V., Tsekeri, A., Gkikas, A., Proestakis, E., Mallios, S., Solomos, S., Spyrou, C.,
1230   Marinou, E., Ryder, C. L., Bouris, D., and Katsafados, P.: Modeling coarse and giant desert dust
         particles, Atmospheric Chemistry and Physics, 22, 12727–12748, https://doi.org/10.5194/acp-22-
         12727-2022, 2022.

Dupont, S., Bergametti, G., Marticorena, B., and Simoëns, S.: Modeling saltation intermittency, Journal
         of Geophysical Research: Atmospheres, 118, 7109–7128, https://doi.org/10.1002/jgrd.50528,
1235   2013.

Emmons, L. K., Schwantes, R. H., Orlando, J. J., Tyndall, G., Kinnison, D., Lamarque, J.-F., Marsh, D.,
         Mills, M. J., Tilmes, S., Bardeen, C., Buchholz, R. R., Conley, A., Gettelman, A., Garcia, R.,
         Simpson, I., Blake, D. R., Meinardi, S., and Pétron, G.: The Chemistry Mechanism in the
         Community Earth System Model Version 2 (CESM2), Journal of Advances in Modeling Earth
1240   Systems, 12, e2019MS001882, https://doi.org/10.1029/2019MS001882, 2020.

ESA: Land Cover CCI Product User Guide Version 2., 2017.

Esmaeil, N., Gharagozloo, M., Rezaei, A., and Grunig, G.: Dust events, pulmonary diseases and immune
         system, Am J Clin Exp Immunol, 3, 20–29, 2014.

Evan, A. T., Fiedler, S., Zhao, C., Menut, L., Schepanski, K., Flamant, C., and Doherty, O.: Derivation
1245   of an observation-based map of North African dust emission, Aeolian Research, 16, 153–162,
         https://doi.org/10.1016/j.aeolia.2015.01.001, 2015.

Feng, Y., Wang, H., Rasch, P. J., Zhang, K., Lin, W., Tang, Q., Xie, S., Hamilton, D. S., Mahowald, N.,
         and Yu, H.: Global Dust Cycle and Direct Radiative Effect in E3SM Version 1: Impact of
         Increasing Model Resolution, Journal of Advances in Modeling Earth Systems, 14,
1250   e2021MS002909, https://doi.org/10.1029/2021MS002909, 2022.

Foroutan, H., Young, J., Napelenok, S., Ran, L., Appel, K. W., Gilliam, R. C., and Pleim, J. E.:
         Development and evaluation of a physics-based windblown dust emission scheme implemented
         in the CMAQ modeling system, Journal of Advances in Modeling Earth Systems, 9, 585–608,
         https://doi.org/10.1002/2016MS000823, 2017.

1255   Froyd, K. D., Yu, P., Schill, G. P., Brock, C. A., Kupc, A., Williamson, C. J., Jensen, E. J., Ray, E.,
         Rosenlof, K. H., Bian, H., Darmenov, A. S., Colarco, P. R., Diskin, G. S., Bui, T., and Murphy,
         D. M.: Dominant role of mineral dust in cirrus cloud formation revealed by global-scale
         measurements, Nat. Geosci., 15, 177–183, https://doi.org/10.1038/s41561-022-00901-w, 2022.

Gaston, C. J.: Re-examining Dust Chemical Aging and Its Impacts on Earth's Climate, Acc. Chem. Res.,
1260   53, 1005–1013, https://doi.org/10.1021/acs.accounts.0c00102, 2020.

Gelaro, R., McCarty, W., Suárez, M. J., Todling, R., Molod, A., Takacs, L., Randles, C. A., Darmenov,
         A., Bosilovich, M. G., Reichle, R., Wargan, K., Coy, L., Cullather, R., Draper, C., Akella, S.,
         Buchard, V., Conaty, A., Silva, A. M. da, Gu, W., Kim, G.-K., Koster, R., Lucchesi, R.,
         Merkova, D., Nielsen, J. E., Partyka, G., Pawson, S., Putman, W., Rienecker, M., Schubert, S.
1265   D., Sienkiewicz, M., and Zhao, B.: The Modern-Era Retrospective Analysis for Research and
         Applications, Version 2 (MERRA-2), Journal of Climate, 30, 5419–5454,
         https://doi.org/10.1175/JCLI-D-16-0758.1, 2017.

Gillette, D. A. and Passi, R.: Modeling dust emission caused by wind erosion, Journal of Geophysical
         Research: Atmospheres, 93, 14233–14242, https://doi.org/10.1029/JD093iD11p14233, 1988.

1270   Ginoux, P., Chin, M., Tegen, I., Prospero, J. M., Holben, B., Dubovik, O., and Lin, S.-J.: Sources and
         distributions of dust aerosols simulated with the GOCART model, Journal of Geophysical
         Research: Atmospheres, 106, 20255–20273, https://doi.org/10.1029/2000JD000053, 2001.

Gkikas, A., Proestakis, E., Amiridis, V., Kazadzis, S., Di Tomaso, E., Tsekeri, A., Marinou, E.,
         Hatzianastassiou, N., and Pérez García-Pando, C.: ModIs Dust AeroSol (MIDAS): a global fine-
1275   resolution dust optical depth data set, Atmos. Meas. Tech., 14, 309–334,
         https://doi.org/10.5194/amt-14-309-2021, 2021.

Gliß, J., Mortier, A., Schulz, M., Andrews, E., Balkanski, Y., Bauer, S. E., Benedictow, A. M. K., Bian, H., Checa-Garcia, R., Chin, M., Ginoux, P., Griesfeller, J. J., Heckel, A., Kipling, Z., Kirkevåg, A., Kokkola, H., Laj, P., Le Sager, P., Lund, M. T., Lund Myhre, C., Matsui, H., Myhre, G., Neubauer, D., van Noije, T., North, P., Olivié, D. J. L., Rémy, S., Sogacheva, L., Takemura, T., Tsigaridis, K., and Tsyro, S. G.: AeroCom phase III multi-model evaluation of the aerosol life cycle and optical properties using ground- and space-based remote sensing as well as surface in situ observations, Atmospheric Chemistry and Physics, 21, 87–128, https://doi.org/10.5194/acp-21-87-2021, 2021.

Gonçalves Ageitos, M., Obiso, V., Miller, R. L., Jorba, O., Klose, M., Dawson, M., Balkanski, Y., Perlwitz, J., Basart, S., Di Tomaso, E., Escribano, J., Macchia, F., Montané, G., Mahowald, N., Green, R. O., Thompson, D. R., and Pérez García-Pando, C.: Modeling dust mineralogical composition: sensitivity to soil mineralogy atlases and their expected climate impacts, EGUsphere, 1–51, https://doi.org/10.5194/egusphere-2022-1414, 2023.

Goudie, A. S.: Desert dust and human health disorders, Environment International, 63, 101–113, https://doi.org/10.1016/j.envint.2013.10.011, 2014.

Green, R. O., Mahowald, N., Ung, C., Thompson, D. R., Bator, L., Bennet, M., Bernas, M., Blackway, N., Bradley, C., Cha, J., Clark, P., Clark, R., Cloud, D., Diaz, E., Ben Dor, E., Duren, R., Eastwood, M., Ehlmann, B. L., Fuentes, L., Ginoux, P., Gross, J., He, Y., Kalashnikova, O., Kert, W., Keymeulen, D., Klimesh, M., Ku, D., Kwong-Fu, H., Liggett, E., Li, L., Lundeen, S., Makowski, M. D., Mazer, A., Miller, R., Mouroulis, P., Oaida, B., Okin, G. S., Ortega, A., Oyake, A., Nguyen, H., Pace, T., Painter, T. H., Pempejian, J., Garcia-Pando, C. P., Pham, T., Phillips, B., Pollock, R., Purcell, R., Realmuto, V., Schoolcraft, J., Sen, A., Shin, S., Shaw, L., Soriano, M., Swayze, G., Thingvold, E., Vaid, A., and Zan, J.: The Earth Surface Mineral Dust Source Investigation: An Earth Science Imaging Spectroscopy Mission, in: 2020 IEEE Aerospace Conference, 2020 IEEE Aerospace Conference, Big Sky, MT, USA, 1–15, https://doi.org/10.1109/AERO47225.2020.9172731, 2020.

Hamilton, D. S., Moore, J. K., Arneth, A., Bond, T. C., Carslaw, K. S., Hantson, S., Ito, A., Kaplan, J. O., Lindsay, K., Nieradzik, L., Rathod, S. D., Scanza, R. A., and Mahowald, N. M.: Impact of Changes to the Atmospheric Soluble Iron Deposition Flux on Ocean Biogeochemical Cycles in the Anthropocene, Global Biogeochemical Cycles, 34, e2019GB006448, https://doi.org/10.1029/2019GB006448, 2020.

Hengl, T., Jesus, J. M. de, Heuvelink, G. B. M., Gonzalez, M. R., Kilibarda, M., Blagotić, A., Shangguan, W., Wright, M. N., Geng, X., Bauer-Marschallinger, B., Guevara, M. A., Vargas, R., MacMillan, R. A., Batjes, N. H., Leenaars, J. G. B., Ribeiro, E., Wheeler, I., Mantel, S., and Kempen, B.: SoilGrids250m: Global gridded soil information based on machine learning, PLOS ONE, 12, e0169748, https://doi.org/10.1371/journal.pone.0169748, 2017.

Holben, B. N., Eck, T. F., Slutsker, I., Tanré, D., Buis, J. P., Setzer, A., Vermote, E., Reagan, J. A., Kaufman, Y. J., Nakajima, T., Lavenu, F., Jankowiak, I., and Smirnov, A.: AERONET—A Federated Instrument Network and Data Archive for Aerosol Characterization, Remote Sensing of Environment, 66, 1–16, https://doi.org/10.1016/S0034-4257(98)00031-5, 1998.

Huang, Y., Kok, J. F., Kandler, K., Lindqvist, H., Nousiainen, T., Sakai, T., Adebiyi, A., and Jokinen, O.: Climate Models and Remote Sensing Retrievals Neglect Substantial Desert Dust Asphericity, Geophysical Research Letters, 47, e2019GL086592, https://doi.org/10.1029/2019GL086592, 2020.

Huang, Y., Adebiyi, A. A., Formenti, P., and Kok, J. F.: Linking the Different Diameter Types of Aspherical Desert Dust Indicates That Models Underestimate Coarse Dust Emission, Geophysical Research Letters, 48, e2020GL092054, https://doi.org/10.1029/2020GL092054, 2021.

1325 Huang, Y., Kok, J. F., Saito, M., and Muñoz, O.: Single-scattering properties of ellipsoidal dust aerosols
         constrained by measured dust shape distributions, Atmospheric Chemistry and Physics, 23,
         2557–2577, https://doi.org/10.5194/acp-23-2557-2023, 2023.
      Ito, A. and Kok, J. F.: Do dust emissions from sparsely vegetated regions dominate atmospheric iron
         supply to the Southern Ocean?, Journal of Geophysical Research: Atmospheres, 122, 3987–
1330   4002, https://doi.org/10.1002/2016JD025939, 2017.
      Iversen, J. D. and White, B. R.: Saltation threshold on Earth, Mars and Venus, Sedimentology, 29, 111–
         119, https://doi.org/10.1111/j.1365-3091.1982.tb01713.x, 1982.
      Kandakji, T., Gill, T. E., and Lee, J. A.: Identifying and characterizing dust point sources in the
         southwestern United States using remote sensing and GIS, Geomorphology, 353, 107019,
1335   https://doi.org/10.1016/j.geomorph.2019.107019, 2020.
      Ke, Z., Liu, X., Wu, M., Shan, Y., and Shi, Y.: Improved Dust Representation and Impacts on Dust
         Transport and Radiative Effect in CAM5, Journal of Advances in Modeling Earth Systems, 14,
         e2021MS002845, https://doi.org/10.1029/2021MS002845, 2022.
      Kinne, S., Schulz, M., Textor, C., Guibert, S., Balkanski, Y., Bauer, S. E., Berntsen, T., Berglen, T. F.,
1340   Boucher, O., Chin, M., Collins, W., Dentener, F., Diehl, T., Easter, R., Feichter, J., Fillmore, D.,
         Ghan, S., Ginoux, P., Gong, S., Grini, A., Hendricks, J., Herzog, M., Horowitz, L., Isaksen, I.,
         Iversen, T., Kirkevåg, A., Kloster, S., Koch, D., Kristjansson, J. E., Krol, M., Lauer, A.,
         Lamarque, J. F., Lesins, G., Liu, X., Lohmann, U., Montanaro, V., Myhre, G., Penner, J., Pitari,
         G., Reddy, S., Seland, O., Stier, P., Takemura, T., and Tie, X.: An AeroCom initial assessment –
1345   optical properties in aerosol component modules of global models, Atmospheric Chemistry and
         Physics, 6, 1815–1834, https://doi.org/10.5194/acp-6-1815-2006, 2006.
      Klose, M. and Shao, Y.: Stochastic parameterization of dust emission and application to convective
         atmospheric conditions, Atmospheric Chemistry and Physics, 12, 7309–7320,
         https://doi.org/10.5194/acp-12-7309-2012, 2012.
1350 Klose, M. and Shao, Y.: Large-eddy simulation of turbulent dust emission, Aeolian Research, 8, 49–58,
         https://doi.org/10.1016/j.aeolia.2012.10.010, 2013.
      Klose, M., Shao, Y., Li, X., Zhang, H., Ishizuka, M., Mikami, M., and Leys, J. F.: Further development
         of a parameterization for convective turbulent dust emission and evaluation based on field
         observations, Journal of Geophysical Research: Atmospheres, 119, 10441–10457,
1355   https://doi.org/10.1002/2014JD021688, 2014.
      Klose, M., Jorba, O., Gonçalves Ageitos, M., Escribano, J., Dawson, M. L., Obiso, V., Di Tomaso, E.,
         Basart, S., Montané Pinto, G., Macchia, F., Ginoux, P., Guerschman, J., Prigent, C., Huang, Y.,
         Kok, J. F., Miller, R. L., and Pérez García-Pando, C.: Mineral dust cycle in the Multiscale Online
         Nonhydrostatic AtmospheRe CHemistry model (MONARCH) Version 2.0, Geosci. Model Dev.,
1360   14, 6403–6444, https://doi.org/10.5194/gmd-14-6403-2021, 2021.
      Kok, J. F.: A scaling theory for the size distribution of emitted dust aerosols suggests climate models
         underestimate the size of the global dust cycle, PNAS, 108, 1016–1021,
         https://doi.org/10.1073/pnas.1014798108, 2011.
      Kok, J. F. and Renno, N. O.: A comprehensive numerical model of steady state saltation (COMSALT),
1365   Journal of Geophysical Research: Atmospheres, 114, https://doi.org/10.1029/2009JD011702,
         2009.
      Kok, J. F., Parteli, E. J. R., Michaels, T. I., and Karam, D. B.: The physics of wind-blown sand and dust,
         Rep. Prog. Phys., 75, 106901, https://doi.org/10.1088/0034-4885/75/10/106901, 2012.
      Kok, J. F., Mahowald, N. M., Fratini, G., Gillies, J. A., Ishizuka, M., Leys, J. F., Mikami, M., Park, M.-
1370   S., Park, S.-U., Van Pelt, R. S., and Zobeck, T. M.: An improved dust emission model – Part 1:
         Model description and comparison against measurements, Atmospheric Chemistry and Physics,
         14, 13023–13041, https://doi.org/10.5194/acp-14-13023-2014, 2014a.

Kok, J. F., Albani, S., Mahowald, N. M., and Ward, D. S.: An improved dust emission model – Part 2: Evaluation in the Community Earth System Model, with implications for the use of dust source functions, Atmospheric Chemistry and Physics, 14, 13043–13061, https://doi.org/10.5194/acp-14-13043-2014, 2014b.

Kok, J. F., Ridley, D. A., Zhou, Q., Miller, R. L., Zhao, C., Heald, C. L., Ward, D. S., Albani, S., and Haustein, K.: Smaller desert dust cooling effect estimated from analysis of dust size and abundance, Nature Geosci, 10, 274–278, https://doi.org/10.1038/ngeo2912, 2017.

Kok, J. F., Adebiyi, A. A., Albani, S., Balkanski, Y., Checa-Garcia, R., Chin, M., Colarco, P. R., Hamilton, D. S., Huang, Y., Ito, A., Klose, M., Leung, D. M., Li, L., Mahowald, N. M., Miller, R. L., Obiso, V., Pérez García-Pando, C., Rocha-Lima, A., Wan, J. S., and Whicker, C. A.: Improved representation of the global dust cycle using observational constraints on dust properties and abundance, Atmos. Chem. Phys., 21, 8127–8167, https://doi.org/10.5194/acp-21-8127-2021, 2021.

Kok, J. F., Storelvmo, T., Karydis, V. A., Adebiyi, A. A., Mahowald, N. M., Evan, A. T., He, C., and Leung, D. M.: Mineral dust aerosol impacts on global climate and climate change, Nat Rev Earth Environ, 1–16, https://doi.org/10.1038/s43017-022-00379-5, 2023.

Laurent, B., Marticorena, B., Bergametti, G., Léon, J. F., and Mahowald, N. M.: Modeling mineral dust emissions from the Sahara desert using new surface properties and soil database, J. Geophys. Res., 113, D14218, https://doi.org/10.1029/2007JD009484, 2008.

LeGrand, S. L., Letcher, T. W., Okin, G. S., Webb, N. P., Gallagher, A. R., Dhital, S., Hodgdon, T. S., Ziegler, N. P., and Michaels, M. L.: Application of a satellite-retrieved sheltering parameterization (v1.0) for dust event simulation with WRF-Chem v4.1, Geoscientific Model Development, 16, 1009–1038, https://doi.org/10.5194/gmd-16-1009-2023, 2023.

Leung, D. M., Tai, A. P. K., Mickley, L. J., Moch, J. M., Donkelaar, A. van, Shen, L., and Martin, R. V.: Synoptic meteorological modes of variability for fine particulate matter ($PM_{2.5}$) air quality in major metropolitan regions of China, Atmospheric Chemistry and Physics, 18, 6733–6748, https://doi.org/10.5194/acp-18-6733-2018, 2018.

Leung, D. M., Kok, J. F., Li, L., Okin, G. S., Prigent, C., Klose, M., Garcia-Pando, C. P., Menut, L., Mahowald, N. M., Lawrence, D. M., and Chamecki, M.: A new process-based and scale-respecting desert dust emission scheme for global climate models – Part I: description and evaluation against inverse modeling emissions, Atmospheric Chemistry and Physics Discussions, 1–58, https://doi.org/10.5194/acp-2022-719, 2022.

Li, L., Mahowald, N. M., Miller, R. L., Pérez García-Pando, C., Klose, M., Hamilton, D. S., Gonçalves Ageitos, M., Ginoux, P., Balkanski, Y., Green, R. O., Kalashnikova, O., Kok, J. F., Obiso, V., Paynter, D., and Thompson, D. R.: Quantifying the range of the dust direct radiative effect due to source mineralogy uncertainty, Atmospheric Chemistry and Physics, 21, 3973–4005, https://doi.org/10.5194/acp-21-3973-2021, 2021.

Li, L., Mahowald, N. M., Kok, J. F., Liu, X., Wu, M., Leung, D. M., Hamilton, D. S., Emmons, L. K., Huang, Y., Sexton, N., Meng, J., and Wan, J.: Importance of different parameterization changes for the updated dust cycle modeling in the Community Atmosphere Model (version 6.1), Geosci. Model Dev., 15, 8181–8219, https://doi.org/10.5194/gmd-15-8181-2022, 2022.

Li, W., MacBean, N., Ciais, P., Defourny, P., Lamarche, C., Bontemps, S., Houghton, R. A., and Peng, S.: Gross and net land cover changes in the main plant functional types derived from the annual ESA CCI land cover maps (1992–2015), Earth System Science Data, 10, 219–234, https://doi.org/10.5194/essd-10-219-2018, 2018.

Liu, X., Ma, P.-L., Wang, H., Tilmes, S., Singh, B., Easter, R. C., Ghan, S. J., and Rasch, P. J.: Description and evaluation of a new four-mode version of the Modal Aerosol Module (MAM4) within version 5.3 of the Community Atmosphere Model, Geosci. Model Dev., 9, 505–522, https://doi.org/10.5194/gmd-9-505-2016, 2016.

Mahowald, N. M., Engelstaedter, S., Luo, C., Sealy, A., Artaxo, P., Benitez-Nelson, C., Bonnet, S.,
Chen, Y., Chuang, P. Y., Cohen, D. D., Dulac, F., Herut, B., Johansen, A. M., Kubilay, N.,
Losno, R., Maenhaut, W., Paytan, A., Prospero, J. M., Shank, L. M., and Siefert, R. L.:
1425   Atmospheric Iron Deposition: Global Distribution, Variability, and Human Perturbations,
Annual Review of Marine Science, 1, 245–278,
https://doi.org/10.1146/annurev.marine.010908.163727, 2009.

Mahowald, N. M., Kloster, S., Engelstaedter, S., Moore, J. K., Mukhopadhyay, S., McConnell, J. R.,
Albani, S., Doney, S. C., Bhattacharya, A., Curran, M. A. J., Flanner, M. G., Hoffman, F. M.,
1430   Lawrence, D. M., Lindsay, K., Mayewski, P. A., Neff, J., Rothenberg, D., Thomas, E., Thornton,
P. E., and Zender, C. S.: Observed 20th century desert dust variability: impact on climate and
biogeochemistry, Atmos. Chem. Phys., 10, 10875–10893, https://doi.org/10.5194/acp-10-10875-
2010, 2010.

Mailler, S., Menut, L., Khvorostyanov, D., Valari, M., Couvidat, F., Siour, G., Turquety, S., Briant, R.,
1435   Tuccella, P., Bessagnet, B., Colette, A., Létinois, L., Markakis, K., and Meleux, F.: CHIMERE-
2017: from urban to hemispheric chemistry-transport modeling, Geoscientific Model
Development, 10, 2397–2423, https://doi.org/10.5194/gmd-10-2397-2017, 2017.

Marticorena, B. and Bergametti, G.: Modeling the atmospheric dust cycle: 1. Design of a soil-derived
dust emission scheme, Journal of Geophysical Research: Atmospheres, 100, 16415–16430,
1440   https://doi.org/10.1029/95JD00690, 1995.

Martin, R. L. and Kok, J. F.: Distinct Thresholds for the Initiation and Cessation of Aeolian Saltation
From Field Measurements, Journal of Geophysical Research: Earth Surface, 123, 1546–1565,
https://doi.org/10.1029/2017JF004416, 2018.

Martin, R. L. and Kok, J. F.: Size-Independent Susceptibility to Transport in Aeolian Saltation, Journal
1445   of Geophysical Research: Earth Surface, 124, 1658–1674,
https://doi.org/10.1029/2019JF005104, 2019.

McGraw, Z., Storelvmo, T., David, R. O., and Sagoo, N.: Global Radiative Impacts of Mineral Dust
Perturbations Through Stratiform Clouds, Journal of Geophysical Research: Atmospheres, 125,
e2019JD031807, https://doi.org/10.1029/2019JD031807, 2020.

1450   Meng, J., Martin, R. V., Ginoux, P., Hammer, M., Sulprizio, M. P., Ridley, D. A., and van Donkelaar,
A.: Grid-independent high-resolution dust emissions (v1.0) for chemical transport models:
application to GEOS-Chem (12.5.0), Geoscientific Model Development, 14, 4249–4260,
https://doi.org/10.5194/gmd-14-4249-2021, 2021.

Meng, J., Huang, Y., Leung, D. M., Li, L., Adebiyi, A. A., Ryder, C. L., Mahowald, N. M., and Kok, J.
1455   F.: Improved Parameterization for the Size Distribution of Emitted Dust Aerosols Reduces
Model Underestimation of Super Coarse Dust, Geophysical Research Letters, 49,
e2021GL097287, https://doi.org/10.1029/2021GL097287, 2022.

Menut, L.: Modeling of Mineral Dust Emissions with a Weibull Wind Speed Distribution Including
Subgrid-Scale Orography Variance, Journal of Atmospheric and Oceanic Technology, 35, 1221–
1460   1236, https://doi.org/10.1175/JTECH-D-17-0173.1, 2018.

Menut, L., Pérez, C., Haustein, K., Bessagnet, B., Prigent, C., and Alfaro, S.: Impact of surface
roughness and soil texture on mineral dust emission fluxes modeling, Journal of Geophysical
Research: Atmospheres, 118, 6505–6520, https://doi.org/10.1002/jgrd.50313, 2013.

Mitroo, D., Gill, T. E., Haas, S., Pratt, K. A., and Gaston, C. J.: ClNO2 Production from N2O5 Uptake
1465   on Saline Playa Dusts: New Insights into Potential Inland Sources of ClNO2, Environ. Sci.
Technol., 53, 7442–7452, https://doi.org/10.1021/acs.est.9b01112, 2019.

Neale, R. B., Gettelman, A., Park, S., Chen, C.-C., Lauritzen, P. H., Williamson, D. L., Conley, A. J.,
Kinnison, D., Marsh, D., Smith, A. K., Vitt, F., Garcia, R., Lamarque, J.-F., Mills, M., Tilmes,
S., Morrison, H., Cameron-Smith, P., Collins, W. D., Iacono, M. J., Easter, R. C., Liu, X., Ghan,

https://doi.org/10.5194/egusphere-2023-823
Preprint. Discussion started: 12 June 2023
© Author(s) 2023. CC BY 4.0 License.

S. J., Rasch, P. J., and Taylor, M. A.: Description of the NCAR Community Atmosphere Model (CAM 5.0), 289, 2012.

Okin, G. S.: A new model of wind erosion in the presence of vegetation, Journal of Geophysical Research: Earth Surface, 113, https://doi.org/10.1029/2007JF000758, 2008.

O'Neill, N. T., Eck, T. F., Smirnov, A., Holben, B. N., and Thulasiraman, S.: Spectral discrimination of coarse and fine mode optical depth, Journal of Geophysical Research: Atmospheres, 108, https://doi.org/10.1029/2002JD002975, 2003.

Petroff, A. and Zhang, L.: Development and validation of a size-resolved particle dry deposition scheme for application in aerosol transport models, Geoscientific Model Development, 3, 753–769, https://doi.org/10.5194/gmd-3-753-2010, 2010.

Philip, S., Martin, R. V., Snider, G., Weagle, C. L., Donkelaar, A. van, Brauer, M., Henze, D. K., Klimont, Z., Venkataraman, C., Guttikunda, S. K., and Zhang, Q.: Anthropogenic fugitive, combustion and industrial dust is a significant, underrepresented fine particulate matter source in global atmospheric models, Environ. Res. Lett., 12, 044018, https://doi.org/10.1088/1748-9326/aa65a4, 2017.

Pierre, C., Bergametti, G., Marticorena, B., Kergoat, L., Mougin, E., and Hiernaux, P.: Comparing drag partition schemes over a herbaceous Sahelian rangeland, Journal of Geophysical Research: Earth Surface, 119, 2291–2313, https://doi.org/10.1002/2014JF003177, 2014.

Prigent, C., Tegen, I., Aires, F., Marticorena, B., and Zribi, M.: Estimation of the aerodynamic roughness length in arid and semi-arid regions over the globe with the ERS scatterometer, Journal of Geophysical Research: Atmospheres, 110, https://doi.org/10.1029/2004JD005370, 2005.

Prigent, C., Jiménez, C., and Catherinot, J.: Comparison of satellite microwave backscattering (ASCAT) and visible/near-infrared reflectances (PARASOL) for the estimation of aeolian aerodynamic roughness length in arid and semi-arid regions, Atmospheric Measurement Techniques, 5, 2703–2712, https://doi.org/10.5194/amt-5-2703-2012, 2012.

Ridley, D. A., Heald, C. L., Pierce, J. R., and Evans, M. J.: Toward resolution-independent dust emissions in global models: Impacts on the seasonal and spatial distribution of dust, Geophysical Research Letters, 40, 2873–2877, https://doi.org/10.1002/grl.50409, 2013.

Ridley, D. A., Heald, C. L., Kok, J. F., and Zhao, C.: An observationally constrained estimate of global dust aerosol optical depth, Atmospheric Chemistry and Physics, 16, 15097–15117, https://doi.org/10.5194/acp-16-15097-2016, 2016.

Rodriguez-Caballero, E., Belnap, J., Büdel, B., Crutzen, P. J., Andreae, M. O., Pöschl, U., and Weber, B.: Dryland photoautotrophic soil surface communities endangered by global change, Nature Geosci, 11, 185–189, https://doi.org/10.1038/s41561-018-0072-1, 2018.

Scanza, R. A., Mahowald, N., Ghan, S., Zender, C. S., Kok, J. F., Liu, X., Zhang, Y., and Albani, S.: Modeling dust as component minerals in the Community Atmosphere Model: development of framework and impact on radiative forcing, Atmospheric Chemistry and Physics, 15, 537–561, https://doi.org/10.5194/acp-15-537-2015, 2015.

Shao, Y. and Lu, H.: A simple expression for wind erosion threshold friction velocity, Journal of Geophysical Research: Atmospheres, 105, 22437–22443, https://doi.org/10.1029/2000JD900304, 2000.

Shao, Y., Ishizuka, M., Mikami, M., and Leys, J. F.: Parameterization of size-resolved dust emission and validation with measurements, Journal of Geophysical Research: Atmospheres, 116, https://doi.org/10.1029/2010JD014527, 2011.

Shao, Y. P., Raupach, M. R., and Leys, J. F.: A model for predicting aeolian sand drift and dust entrainment on scales from paddock to region, Soil Res., 34, 309–342, https://doi.org/10.1071/sr9960309, 1996.

Storelvmo, T.: Aerosol Effects on Climate via Mixed-Phase and Ice Clouds, Annual Review of Earth
    and Planetary Sciences, 45, 199–222, https://doi.org/10.1146/annurev-earth-060115-012240,
1520   2017.
Tai, A. P. K., Ma, P. H. L., Chan, Y.-C., Chow, M.-K., Ridley, D. A., and Kok, J. F.: Impacts of climate
    and land cover variability and trends on springtime East Asian dust emission over 1982–2010: A
    modeling study, Atmospheric Environment, 254, 118348,
    https://doi.org/10.1016/j.atmosenv.2021.118348, 2021.
1525 Tang, M., Huang, X., Lu, K., Ge, M., Li, Y., Cheng, P., Zhu, T., Ding, A., Zhang, Y., Gligorovski, S.,
    Song, W., Ding, X., Bi, X., and Wang, X.: Heterogeneous reactions of mineral dust aerosol:
    implications for tropospheric oxidation capacity, Atmospheric Chemistry and Physics, 17,
    11727–11777, https://doi.org/10.5194/acp-17-11727-2017, 2017.
Thompson, D. R., Braverman, A., Brodrick, P. G., Candela, A., Carmon, N., Clark, R. N., Connelly, D.,
1530   Green, R. O., Kokaly, R. F., Li, L., Mahowald, N., Miller, R. L., Okin, G. S., Painter, T. H.,
    Swayze, G. A., Turmon, M., Susilouto, J., and Wettergreen, D. S.: Quantifying uncertainty for
    remote spectroscopy of surface composition, Remote Sensing of Environment, 247, 111898,
    https://doi.org/10.1016/j.rse.2020.111898, 2020.
Wang, J., Xu, X., Henze, D. K., Zeng, J., Ji, Q., Tsay, S.-C., and Huang, J.: Top-down estimate of dust
1535   emissions through integration of MODIS and MISR aerosol retrievals with the GEOS-Chem
    adjoint model, Geophysical Research Letters, 39, https://doi.org/10.1029/2012GL051136, 2012.
Wang, Y., Xia, W., Liu, X., Xie, S., Lin, W., Tang, Q., Ma, H.-Y., Jiang, Y., Wang, B., and Zhang, G.
    J.: Disproportionate control on aerosol burden by light rain, Nat. Geosci., 14, 72–76,
    https://doi.org/10.1038/s41561-020-00675-z, 2021.
1540 Weinzierl, B., Ansmann, A., Prospero, J. M., Althausen, D., Benker, N., Chouza, F., Dollner, M.,
    Farrell, D., Fomba, W. K., Freudenthaler, V., Gasteiger, J., Groß, S., Haarig, M., Heinold, B.,
    Kandler, K., Kristensen, T. B., Mayol-Bracero, O. L., Müller, T., Reitebuch, O., Sauer, D.,
    Schäfler, A., Schepanski, K., Spanu, A., Tegen, I., Toledano, C., and Walser, A.: The Saharan
    Aerosol Long-Range Transport and Aerosol–Cloud-Interaction Experiment: Overview and
1545   Selected Highlights, Bulletin of the American Meteorological Society, 98, 1427–1451,
    https://doi.org/10.1175/BAMS-D-15-00142.1, 2017.
White, B. R.: soil transport by winds on Mars, Journal of Geophysical Research: Solid Earth, 84, 4643–
    4651, https://doi.org/10.1029/JB084iB09p04643, 1979.
Wu, C., Lin, Z., Liu, X., Ji, D., Zhang, H., Li, C., and Lin, G.: Description of Dust Emission
1550   Parameterization in CAS-ESM2 and Its Simulation of Global Dust Cycle and East Asian Dust
    Events, Journal of Advances in Modeling Earth Systems, 13, e2020MS002456,
    https://doi.org/10.1029/2020MS002456, 2021.
Wu, M., Liu, X., Yu, H., Wang, H., Shi, Y., Yang, K., Darmenov, A., Wu, C., Wang, Z., Luo, T., Feng,
    Y., and Ke, Z.: Understanding processes that control dust spatial distributions with global
1555   climate models and satellite observations, Atmospheric Chemistry and Physics, 20, 13835–
    13855, https://doi.org/10.5194/acp-20-13835-2020, 2020.
Xia, W., Wang, Y., Chen, S., Huang, J., Wang, B., Zhang, G. J., Zhang, Y., Liu, X., Ma, J., Gong, P.,
    Jiang, Y., Wu, M., Xue, J., Wei, L., and Zhang, T.: Double Trouble of Air Pollution by
    Anthropogenic Dust, Environ. Sci. Technol., 56, 761–769,
1560   https://doi.org/10.1021/acs.est.1c04779, 2022.
Zender, C. S., Bian, H., and Newman, D.: Mineral Dust Entrainment and Deposition (DEAD) model:
    Description and 1990s dust climatology, Journal of Geophysical Research: Atmospheres, 108,
    https://doi.org/10.1029/2002JD002775, 2003a.
Zender, C. S., Newman, D., and Torres, O.: Spatial heterogeneity in aeolian erodibility: Uniform,
1565   topographic, geomorphic, and hydrologic hypotheses, Journal of Geophysical Research:
    Atmospheres, 108, https://doi.org/10.1029/2002JD003039, 2003b.

Zhang, L., Gong, S., Padro, J., and Barrie, L.: A size-segregated particle dry deposition scheme for an atmospheric aerosol module, Atmospheric Environment, 35, 549–560, https://doi.org/10.1016/S1352-2310(00)00326-5, 2001.

1570 Zhang, L., Kok, J. F., Henze, D. K., Li, Q., and Zhao, C.: Improving simulations of fine dust surface concentrations over the western United States by optimizing the particle size distribution, Geophysical Research Letters, 40, 3270–3275, https://doi.org/10.1002/grl.50591, 2013.

Zhao, A., Ryder, C. L., and Wilcox, L. J.: How well do the CMIP6 models simulate dust aerosols?, Atmospheric Chemistry and Physics, 22, 2095–2119, https://doi.org/10.5194/acp-22-2095-2022,

1575 2022.

Zuidema, P., Alvarez, C., Kramer, S. J., Custals, L., Izaguirre, M., Sealy, P., Prospero, J. M., and Blades, E.: Is Summer African Dust Arriving Earlier to Barbados? The Updated Long-Term In Situ Dust Mass Concentration Time Series from Ragged Point, Barbados, and Miami, Florida, Bulletin of the American Meteorological Society, 100, 1981–1986,

1580 https://doi.org/10.1175/BAMS-D-18-0083.1, 2019.